Severity of arterial defects in the retina correlates with the burden of intracerebral haemorrhage in COL4A1-related stroke

Julien Ratelade, Nicolas Mezouar, Valérie Domenga-Denier, Ambre Rochey, Emmanuelle Plaisier, Anne Joutel

Severity of arterial defects in the retina correlates with the burden of intracerebral hemorrhage in COL4A1-related stroke

Julien Ratelade[1], Nicolas Mezouar[1], Valérie Domenga-Denier[1], Ambre Rochey[1], Emmanuelle Plaisier[2,3] and Anne Joutel[1,4]

Author information

[1]Genetics and Pathogenesis of Cerebrovascular Diseases, INSERM, Université Paris Diderot-Paris 7, Paris, France

[2]Department of Nephrology and Dialysis, AP-HP, Hôpital Tenon, Paris, France

[3]From Rare and Common Kidney Diseases, Remodeling and Repair, INSERM, Sorbonne Universités, Université Pierre et Marie Curie-Paris 6, Paris, France

[4]DHU NeuroVasc, Sorbonne Paris Cité, Paris, France

Corresponding author: Anne Joutel

Email: anne.joutel@inserm.fr

Tel: +33 1 57 27 85 93

Fax: +33 1 57 27 85 94

Conflict of interest

The authors declare that they have no conflicts of interest.

Running title: Smooth muscle cell loss in COL4A1-related stroke

ABSTRACT

Mutations in α1 (COL4A1) or α2 (COL4A2) chains of collagen type IV, a major component of the vascular basement membrane, cause intracerebral hemorrhages with variable expressivity and reduced penetrance by mechanisms that remain poorly understood. Here we sought to investigate the cellular mechanisms of COL4A1-related intracerebral hemorrhage and identify a marker for hemorrhage risk stratification. A combination of histological, immunohistochemical and electron microscopy analyses were used to analyze the brain parenchyma, cerebrovasculature, and retinal vessels of mice expressing the disease-causing COL4A1 p.G498V mutation. Mutant mice developed cerebral microhemorrhages and macroscopic hemorrhages (macrohemorrhages), the latter with reduced penetrance, mimicking the human disease. Microhemorrhages that occurred in early postnatal life were associated with a transient, generalized increase in blood-brain barrier permeability at the level of capillaries. Macrohemorrhages, which occurred later in life, originated from deep brain arteries with focal loss of smooth muscle cells. Similar smooth muscle cell loss was detected in retinal arteries, and a time-course analysis of arterial lesions showed that smooth muscle cells are recruited normally in arterial wall during development, but undergo progressive apoptosis-mediated degeneration. By assessing in parallel the extent of these retinal arterial lesions and the presence/absence of macrohemorrhages, we found that the arterial lesion load in the retina is strongly correlated with the burden of macrohemorrhages. We conclude that microhemorrhages and macrohemorrhages are driven by two distinct mechanisms. Moreover smooth muscle cell degeneration is a critical factor underlying the partial penetrance of COL4A1-related macrohemorrhages, and retinal imaging is a promising tool for identifying high-risk patients.

Keywords: COL4A1, COL4A2, intracerebral hemorrhage, basement membrane, smooth muscle cell, retinal imaging.

Introduction

Spontaneous intracerebral hemorrhage (ICH, or macroscopic hemorrhage) accounts for 10–15% of strokes, but is the most devastating subtype of stroke with high rates of death and long-term disability [1]. Hypertension, currently considered the most important risk factor for ICH, results in hemorrhages in deep brain regions. There is mounting evidence that *COL4A1* and *COL4A2* genes, which encode α1 and α2 chains of collagen type IV, respectively, play a substantial role in the pathogenesis of deep ICH. Common variations in the genomic region of human *COL4A1* and *COL4A2* genes, located in tandem on chromosome 13, confer risk for sporadic forms of deep ICH [2]. In addition, dominant mutations in *COL4A1* or *COL4A2* cause a monogenic form of deep ICH that is associated with a large spectrum of renal, ocular, and skeletal anomalies [3]. Notably, the severity of bleeding within the brain parenchyma is highly variable, both within and between families, and ranges from asymptomatic microbleeds detected by magnetic resonance imaging (MRI) to life-threatening macroscopic hemorrhages [4]. Importantly, clinical studies have revealed that less than 15% of *COL4A1/COL4A2* mutation carriers develop ICH over the course of their lifetimes [5].

Collagen type IV α1 and α2 chains are major components of vascular basement membranes (BMs). Two α1 and one α2 chains assemble into heterotrimers within the endoplasmic reticulum before being secreted to the BM [6]. The most prevalent *COL4A1/COL4A2* mutations are glycine substitutions in the conserved Gly-X-Y motifs within the triple-helical collagenous domain. Previous studies have shown that heterotrimers incorporating mutant COL4A1 or COL4A2 chains tend to accumulate intracellularly in vascular cells, and have proposed that the cytotoxic endoplasmic reticulum (ER) stress associated with this intracellular accumulation, on top of an abnormal angiogenesis, underlies ICH [7]. Yet, our understanding of the pathological processes underlying ICH is still limited. Moreover, although genetic and environmental factors, such as physical exercise and anticoagulant therapy, have been shown to increase the

risk of hemorrhage [7], a satisfactory mechanistic explanation for the reduced penetrance of ICH is lacking. As a consequence, clinical management of mutation carriers remains challenging; accordingly, a predictive marker of ICH would be highly desirable.

The COL4A1 G498V mutation has been previously identified in a human family with cerebral bleeds, renal cysts, muscle cramps, and retinal arterial tortuosity [8,9]. Recent studies indicate that G498V mutant mice are viable and similarly develop renal cysts, muscular dystrophy and retinal arterial tortuosity [10–12], suggesting that this knock-in mouse model represents a valuable and relevant model for studying the pathogenesis of COL4A1 disease.

In this study, we characterized the hemorrhagic phenotype produced by the COL4A1 G498V mutation. To gain insight into the mechanisms of ICH, we studied the pathological changes of cerebral and retinal vessels. We then investigated whether retinal vascular imaging could be used as a screening tool to predict the risk of ICH in mutant mice.

Materials and methods

Detailed information about RNA preparation, immunohistochemistry, transmission electron microscopy procedure, quantitative analysis and antibodies is available in supplementary methods.

Mice

The *Col4a1* G498V mouse line was established by homologous recombination, as previously described [10]. To generate *Col4a1* G498V mice, we first crossed *Col4a1*$^{+/G498V}$ males (100% C57BL/6) with wild-type females (100% 129/Sv), after which *Col4a1*$^{+/G498V}$ mice (50% C57BL/6:50% 129/Sv) were bred together. The mice used in this study—*Col4a1*$^{+/+}$, *Col4a1*$^{+/G498V}$ and *Col4a1*$^{G498V/G498V}$ mice—were littermates with the same hybrid background (50% C57BL/6:50% 129/Sv). Experiments were conducted in full accordance with the guidelines of our local institutional Animal Care and Use Committee (Lariboisiere-Villemin, CEA9).

Perl's staining

Mice were deeply anesthetized with sodium pentobarbital (80 mg/kg) and transcardially perfused with phosphate-buffered saline (PBS). The brain was removed, fixed in 4% paraformaldehyde (PFA) overnight, and cut into 50-µm-thick sagittal sections using a vibratome. Sections were incubated in a 2% hydrochloric acid/2% potassium ferrocyanide solution for 15 minutes and were imaged using a microscope-mounted Nikon DXM1200 digital camera.

Statistics

Unless specified otherwise, data in figures and text are presented as means ± standard error of the mean. Statistical significance was determined using either Student's t-test, one-way analysis of variance (ANOVA) followed by Tukey's post hoc test, or Kruskal-Wallis test followed by Dunn's post hoc test, as specified in figure legends (GraphPad Prism 6 software). Chi-square and Fisher exact tests were used to compare the penetrance of macrohemorrhages between different groups. Correlation analyses were performed using the Spearman test.

Results

Col4a1 G498V mutant mice exhibit highly penetrant microhemorrhages and macroscopic hemorrhages with reduced penetrance that develop along markedly different time courses.

We first characterized the hemorrhagic phenotype produced by the COL4A1 G498V mutation. Heterozygous *Col4a1*$^{+/G498V}$ mice were born at the expected Mendelian ratios and were viable, whereas homozygous *Col4a1*$^{G498V/G498V}$ mice showed reduced viability, with 20% and 28.5% lethality at weaning and 3 months of age, respectively. At 1 month, *Col4a1*$^{+/G498V}$ mice exhibited numerous, small, round foci of fresh bleeds as well as discrete hemosiderin deposits indicative of previous bleeds scattered throughout the brain (Figure 1A). These lesions had a mean diameter of 47 ± 20 (S.D.) µm (range, 25–138 µm, n = 7774 bleeds analyzed in 19 *Col4a1*$^{+/G498V}$ mice) and will be referred to here as microhemorrhages (microh). Microh were associated with small foci of CD68-positive, activated microglia/macrophages intermingled with reactive GFAP (glial fibrillary acidic protein)-positive astrocytes (Figure 1B). Microh were present in all *Col4a1*$^{+/G498V}$ mice, although their numbers were variable (mean number/animal, 409 ± 43; Figure 1C). Microh were almost completely cleared in *Col4a1*$^{+/G498V}$ mice by 3 months (mean number/animal, 5 ± 1); however, at this time, large, well-delineated, dark blue hemosiderin deposits, and more rarely large fresh bleeds, appeared in deep brain

regions, including the thalamus, brainstem, and cerebellum (Figure 1A). These macroscopic hemorrhages, which we have termed macrohemorrhages (macroH) had a mean diameter of 269 ± 80 (S.D.) µm (range 202–462 µm, n = 9 bleeds) and consisted of a dense core of CD68-positive cells surrounded by a large rim of GFAP-positive reactive astrocytes, forming a glial scar (Figure 1B). MacroH were present in only 20% and 26% of *Col4a1*$^{+/G498V}$ mice at 3 and 6 months, respectively, and their number did not exceed 3 per mouse (Figure 1D).

Col4a1$^{G498V/G498V}$ mice were also analyzed at 1 and 3 months and presented with a phenotype similar to that of *Col4a1*$^{+/G498V}$ mice, with numerous microh at 1 month and only a few macroH at 3 months (Figure S1). However, both the penetrance (36%) and number (1–12) of macroH were higher in *Col4a1*$^{G498V/G498V}$ mice compared with age-matched *Col4a1*$^{+/G498V}$ mice (Figure S1). Collectively, our data indicate that *Col4a1* G498V mice mimic the human disease, especially with respect to the variable expressivity of bleeding and reduced penetrance of macroH.

Col4a1 G498V mutant mice exhibit structural defects in the endothelial and smooth muscle BMs and a dose-dependent reduction in BM levels of COL4A1 and COL4A2

We first assessed the effect of COL4A1 G498V mutation on brain vascular BMs using transmission electron microscopy (TEM) in adult mice. Compared with wildtype mice, endothelial-pericyte BMs at the level of capillaries, and BMs surrounding SMCs at the level of arteries (smooth muscle BMs), were thinner with fuzzy edges and occasional focal interruptions in *Col4a1*$^{+/G498V}$ mice (Figure S2).

We next investigated the effect of COL4A1 G498V mutation on the localization and levels of the α1 (COL4A1) chain using a monoclonal antibody to the C-terminal domain of COL4A1, in combination with the BM marker heparan sulfate proteoglycan core protein (perlecan), and the smooth muscle cell (SMC) marker, smooth muscle α-actin (α-SMA). To disentangle the effect

of mutant and wildtype COL4A1 chains, we analyzed *Col4a1*$^{G498V/G498V}$ mice in addition to *Col4a1*$^{+/G498V}$ mice. High-magnification confocal microscopy showed a uniform distribution of COL4A1 at endothelial-pericyte and smooth muscle BMs in both heterozygous and homozygous mutant mice as seen by colocalization with perlecan, with no evidence of intracellular accumulation of COL4A1 (Figure S3A-C). Consistent with this observation, quantitative reverse transcription-polymerase chain reaction performed on isolated brain vessels from *Col4a1*$^{+/G498V}$ mice revealed no change in the level of the ER stress-induced genes coding for C/EBP homologous protein (CHOP), glucose-regulated protein 78 (GRP78) and X-box–binding protein 1 spliced (sXBP1) in mutant mice (Figure S4). However, the intensity of COL4A1 immunofluorescence was significantly reduced along endothelial-pericyte BMs, at the level of capillaries, in *Col4a1*$^{+/G498V}$ mice compared with *Col4a1*$^{+/+}$ mice (Figure S3B, D). Of interest, this reduction was even more pronounced in *Col4a1*$^{G498V/G498V}$ mice compared with *Col4a1*$^{+/G498V}$ mice (Figure S3D). There was also a trend towards a reduction in COL4A1 staining along smooth muscle BMs, at the level of arteries, in mutant mice, although this did not reach statistical significance (Figure S3C, D).

We then examined whether the expression level of the α2 (COL4A2) chain, which assembles with two α1 chains into heterotrimers, was also affected. Notably, COL4A2 staining was significantly reduced along endothelial-pericyte BMs and to a lower extent along smooth muscle BMs in *Col4a1*$^{+/G498V}$ mice, and COL4A2 labeling was even further reduced in *Col4a1*$^{G498V/G498V}$ brain vessels (Figure S3E, F).

To investigate whether other collagen IV isoforms may compensate for the altered levels of the α1α1α2 (IV) trimer, we assessed the levels of α3α4α5 and α5α5α6 (IV) trimers using monoclonal antibodies against COL4A3 and COL4A6, respectively. In *Col4a1*$^{+/+}$ mice, COL4A3 was only expressed in choroid plexus BMs, and COL4A6, which is expressed in the

BMs pia mater, was detected only around arteries as previously reported [13]. Importantly, no *de novo* expression of COL4A3 was observed in *Col4a1*$^{+/G498V}$ mice, and COL4A6 had comparable levels in *Col4a1*$^{+/G498V}$ and *Col4a1*$^{+/+}$ mice (Figure S5). Collectively, these data indicate that the G498V mutation compromises the structural integrity of brain vascular BMs and causes a dose-dependent reduction in the levels of COL4A1 and COL4A2 in BMs of cerebral vessels, which is not compensated by other collagen IV isoforms.

Microh are associated with a transient increase in BBB permeability

We next investigated the pathological changes responsible for cerebral bleeding. Our above findings indicate that microh and macroH may represent separate pathophysiological events. We first sought to localize the sites of microh by triple-immunostaining brains from 1-month-old mutant mice using the markers, hemoglobin α (Hbα) for red blood cells (RBCs), α-SMA for SMCs, and perlecan for BMs. Vessels were classified according to the criteria of Hill and colleagues [14]: arteries/arterioles were defined as vessels covered by α-SMA-positive SMCs independently of their size, capillaries as α-SMA-negative vessels with a diameter ranging from 3 to 9 µm, and veins/venules as α-SMA-negative vessels with a diameter greater than 9 µm. An analysis of 45 randomly selected microh (n = 3 mice) revealed that RBCs were predominantly located around capillaries and, to a lesser extent, around post-capillary venules (Figure 2A, B). Diffuse brain hemorrhages have been previously attributed to a dysfunctional BBB [15,16]. Therefore, we investigated the integrity of the BBB by monitoring extravasation of Evans blue and fluorescein isothiocyanate-labeled albumin (FITC-albumin) tracers and endogenous immunoglobulins (IgGs), which normally do not cross the BBB. At 1 month, we found a massive, diffuse leakage of Evans blue in the brains of *Col4a1*$^{+/G498V}$ mice that was absent in *Col4a1*$^{+/+}$ mice (Figure 2C). Remarkably, at 3 months, extravasation of Evans blue was no longer detected in mutant brains (Figure 2C), except rarely in areas of recent macroH (not

shown). Identical results were found using FITC-albumin tracer and endogenous IgGs (Figure 2D). Similarly, a diffuse increased permeability of the BBB was observed in *Col4a1*$^{G498V/G498V}$ mice at one month but not at 3 months (Figure S6).

It has been shown previously that pericytes play a critical role in the formation and maintenance of BBB integrity [17]. However, we found that pericyte coverage of capillaries, assessed by immunostaining for the platelet-derived growth factor receptor-β (PDGFRβ) pericyte marker, was comparable between *Col4a1*$^{+/G498V}$ and *Col4a1*$^{+/+}$ mice (Figure S7).

Altogether, these data show that microh mostly occur at the level of capillaries and are associated with a generalized, but transient, increase in BBB permeability.

MacroH originate from deep brain arteries and are associated with focal and segmental SMC loss

We next sought to identify the hemorrhagic vessels within macroH in 3-month-old mutant mice. Brain samples from *Col4a1*$^{+/G498V}$ and *Col4a1*$^{G498V/G498V}$ mice containing recent macroH were processed in their entirety into 10-µm-thick cryosections and immunostained for nuclei (DAPI), endogenous IgG or Hbα, α-SMA and elastin, a component of the elastic lamina of artery. Fluorescence microscopy analyses showed that fresh macroH, identified by light microscopy or by reduced density of nuclei, likely as a result of the presence of blood, were centered around vessels exhibiting robust Hbα staining or strong endogenous IgG deposits within and around the vessel wall (Figure 3A and S8). All "hemorrhagic" vessels were identified as arteries, as evidenced by their positive staining for α-SMA or elastin. More importantly, α-SMA and elastin staining in these hemorrhagic arteries was strongly reduced and discontinuous compared with that in control arteries, indicating disruption of the arterial wall (Figure 3A and S8).

Next, we examined the ultrastructure of hemorrhagic blood vessels associated with macroH, identified beforehand on semi-thin sections by light microscopy. TEM confirmed that blood was deposited around arteries in mutant mice, and that these arteries had a highly disorganized wall (Figure 3B). Indeed, whereas SMCs of control arteries constituted one continuous, regular layer of elongated cells, SMC coverage of hemorrhagic arteries was discontinuous, and the remaining SMCs were fragmented or noticeably thinner.

To determine if these SMC defects were causally related to the occurrence of macroH or were the result of toxic effects of blood breakdown products, we examined whether brain arteries at a distance from macroH were also altered. An analysis of 100-µm-thick brain sections, which allowed visualization of long arterial segments, revealed patchy loss of α-SMA staining along medium-sized (10–50 µm diameter) penetrating arteries within deep brain regions in *Col4a1*$^{+/G498V}$ mice (Figure 4A). TEM revealed focal and segmental loss in the SMC coat of the deep brain arteries that left the endothelial cells in direct contact with the brain parenchyma (Figure 4B). SMCs with altered morphology, including rounded cells and cells with a thinner cytoplasm and reduced number of dense plaques, were also observed (Figure 4B, C). Collectively, these results suggest that focal and segmental loss of SMCs in deep brain arteries is involved in macroH in *Col4a1* G498V mutant mice.

Retinal arteries of *Col4a1* G498V mutant mice exhibit similar SMC defects

Retinal vessels share many properties with cerebral vessels [18], prompting us to examine whether retinal arteries from *Col4a1* G498V mutant mice exhibit similar defects to those observed in cerebral arteries. Flat-mounted retinas (Figure 5A) were prepared from wild-type and mutant mice at 3 months of age, a time when the latter develop macroH, and immunostained for α-SMA and perlecan. Focal and segmental SMC abnormalities highly reminiscent of those observed in deep brain arteries were apparent in *Col4a1*$^{+/G498V}$ and *Col4a1*$^{G498V/G498V}$ retinal

arteries (Figures 5B and S9A). SMC defects were detected on proximal arteries (diameter, 20–40 μm) and consisted of patchy gaps of SMCs (Figures 5B and S9A). Notably, measurements of the lengths of arterial segments with SMC defects showed that arterial defects were more pronounced in *Col4a1*$^{G498V/G498V}$ mice compared with age-matched *Col4a1*$^{+/G498V}$ mice (Figure S9B). Costaining for nuclei and α-SMA further showed that SMCs were lost in mutant arteries rather than just losing α-SMA expression (Figure S9C).

Arterial SMCs are recruited normally in *Col4a1* G498V mutant mice, but undergo progressive degeneration

We took advantage of the flat-mounted retina preparation in which, unlike the brain, the arterial tree is nearly planar and has a stereotyped organization (Figure 5A), to investigate the cellular mechanisms underlying SMC abnormalities. An analysis of the time course of arterial lesion development revealed comparable α-SMA staining in *Col4a1*$^{+/G498V}$ and *Col4a1*$^{+/+}$ mice at 1 month of age, but showed a gradual progression of lesions beyond that time, with the percentage of arterial beds exhibiting SMC defects increasing from 2.7% at 3 months to 7.2% at 6 months (Figure 5B, C).

To assess whether loss of α-SMA staining reflected a switch of SMCs to a less differentiated synthetic phenotype or, alternatively, a degenerative process, we stained retinas of *Col4a1* G498V mutant mice and aged-matched controls for α-SMA, the undifferentiated mesenchymal marker PDGFRβ, and the apoptosis marker cleaved caspase-3. No PDGFRβ-positive cells were detected within α-SMA gaps (Figure 5D), arguing against dedifferentiation of mutant SMCs, but the number of caspase-3–positive cells detected in mutant retinal vessels was significantly increased suggesting that loss of mutant SMCs is mediated by apoptosis in *Col4a1*$^{+/G498V}$ mice (Figure 5E, F). Similar findings were observed in *Col4a1*$^{G498V/G498V}$ mice (Figure S9D-F).

Collectively, our data indicate that the COL4A1 G498V mutation does not impair mural cell recruitment or differentiation, but causes progressive degeneration of arterial SMCs.

The severity of arterial SMC loss in the retina correlates with macroH burden

Retinal vascular imaging represents a promising screening tool for evaluating cerebrovascular diseases in humans [18]. Accordingly, we asked whether scoring the arterial lesion load in the retina could be used as a risk marker for macroH. Such an approach would be within reach in humans owing to revolutionary changes in retinal imaging made possible by the use of adaptive optics technology [19]. To achieve this, we investigated the relationship between the extent of SMCs loss in retinal arteries and the burden of macroH in cross-sectional analyses; macroH and SMC defects were quantified by two different investigators blinded to group-identifying information. The data above showed that *Col4a1*$^{G498V/G498V}$ mice exhibit a more severe hemorrhagic phenotype, hence we used a cohort of 14 *Col4a1*$^{G498V/G498V}$ mice for an initial analysis. We found that SMC loss was significantly more severe in the subgroup of *Col4a1*$^{G498V/G498V}$ mice with macroH (26.4% ± 3.7%) compared with those without macroH (5.5% ± 0.9%), and that *Col4a1*$^{G498V/G498V}$ mice with macroH had an arterial lesion load greater than 15% (Figure 6A, B). Moreover, the extent of SMC loss in *Col4a1*$^{G498V/G498V}$ mice was significantly correlated (r = 0.83) with the number of macroH (Figure 6C).

Since *COL4A1* mutations are expressed in a heterozygous state in humans, we next analyzed a cohort of *Col4a1*$^{+/G498V}$ mice. Mutant mice (n = 45) aged 6 months were stratified into three groups, each consisting of 15 mice, according to the severity of SMC defects, and the prevalence of macroH was determined within each group. In group I –marginal SMC defects– (< 2.2% of total length), only 6.6% of *Col4a1*$^{+/G498V}$ mice had macroH (Figure 6D). The prevalence of macroH increased in group II mice –moderate SMC defects– (2.3% to 7.8% of total length) and reached 66.6% in group III –severe SMC defects– (> 7.9% of total length).

Statistical analyses showed that the increasing prevalence of macroH according to the severity of SMC defects was highly significant ($P = 0.0018$, chi-square test). Taken together, these findings suggest that the arterial-lesion–load score in the retina is a promising marker for macroH risk stratification.

Discussion

Although it has been a decade since mutations in COL4A1 were shown to cause ICH in humans and mice, it is still unknown how and why ICH occurs. Here, using meticulous histological, immunohistochemical and electron microscopy analyses of the brain parenchyma, cerebrovasculature and retinal vessels of a mouse model expressing a COL4A1 disease-causing mutation, we provide major new insights into the pathological processes underlying ICH associated with COL4A1 mutations and identify a promising marker for ICH risk stratification.

We found that *Col4a1* G498V mutant (heterozygous and homozygous) mice develop numerous microh in early postnatal life that were almost completely cleared with age, whereas a few macroH appeared with age in deep regions of the brain. A similar pattern of microh and macroH has recently been reported in the extensively studied *Col4a1*$^{+/\Delta ex41}$ model, and was interpreted as reflecting a single continuum of hemorrhage sizes at distinct stages of the disease [7]. We now provide evidence that microh and macroH represent distinct pathophysiological events. Microh occur at the level of capillaries and are associated with a generalized but transient increase in BBB permeability. The surge of microh and the transient BBB leakage that occur during the first month of life in mutant mice suggest a defect in the remodeling of the cerebrovascular network that normally occurs in the mouse brain during this period [20]. On the other hand, our data suggest that macroH arise from weakening and rupture of the wall of deep brain arteries due to age-related focal and segmental SMC degeneration, although further studies are needed to establish the causality between SMC loss and macroH. Similar SMC degeneration in arteries and arterioles has been previously described in ICH associated with hypertension and cerebral amyloid angiopathy, suggesting a central role for SMC defects in spontaneous ICH [21–24]. Investigation of other *Col4a1* mouse models is warranted to confirm that similar mechanisms operate with other *COL4A1* mutations, although the observation that *Col4a1*$^{+/\Delta ex41}$ mice exhibit a similar pattern of microh and macroH suggests that the mechanisms

described above are not specific to the G498V mutation [7]. Notably, our finding that microh and macroH represent distinct entities should be taken into consideration in future preclinical studies. Indeed, genetic manipulations or therapies may affect microh and macroH differently, and assessing their impact without explicitly differentiating between them may prevent meaningful conclusions from being drawn.

Clinical studies have shown that cerebral bleeds in patients with COL4A1 or COL4A2 mutations range in severity from asymptomatic microbleeds detected by MRI to life-threatening macroscopic hemorrhage. Although it is not entirely clear whether microbleeds in humans correspond to what we have defined as "microh" in the mouse, our findings suggest that microbleeds and macroscopic hemorrhages are two distinct, independent events in COL4A1/2 patients and predict that microbleeds are probably not a risk marker for macroscopic hemorrhage. This is important, given that the significance of microbleeds in defining the risk for future macroscopic hemorrhage is an active area of ongoing research [25]. Further analyses of the relationship between these two events in longitudinal studies are warranted to confirm this prediction.

In the present study, we did not find evidence of intracellular accumulation of collagen type IV nor of ER stress in the cerebrovasculature of mutant mice. The G498V mutation is a typical glycine substitution in the conserved Gly-X-Y motifs within the amino-terminal half of COL4A1. Hence, our findings are consistent with *in vitro* studies showing that glycine substitutions in the amino-terminal half of the protein cause milder or even no intracellular accumulation [26]. On the other hand, *Col4a1* G498V mutant mice, which also develop a type of muscular dystrophy, exhibit intracellular accumulation of COL4A1-COL4A2 heterotrimers in the endothelial cells of skeletal muscle capillaries that is associated with major structural abnormalities of the ER and activation of the unfolded protein response [11]. Therefore, these

data suggest that the effect of COL4A1 mutations on collagen IV formation and secretion can be tissue and cell-context dependent in addition to be position-dependent. Cellular specificity of the consequences of COL4A1 mutations on secretion and ER stress was previously reported in animal models of COL4A1-related renal disease [27].

Importantly, we found that BM levels of COL4A1 and COL4A2 were reduced in the cerebral vessels of heterozygous mutant mice, a reduction that was not compensated by other collagen IV isoforms and was even more pronounced in homozygous mutant mice, which exhibited a more severe hemorrhagic phenotype. The reduction of both COL4A1 and COL4A2 levels may be related to impaired assembly or altered stability/enhanced degradation of $\alpha1\alpha1\alpha2$ heterotrimers containing mutant $\alpha1$ chains. Although we cannot formally exclude a subtle or transient intracellular accumulation of mutant collagen in the cerebrovasculature that might have gone undetected by our confocal microscopy analysis, our results suggest that ICH is driven by a BM deficiency of COL4A1-COL4A2 in *Col4a1* G498V mice. Supporting this mechanism, COL4A1 frameshift or splice site mutations associated with a reduction in COL4A1 mRNA and protein levels have been identified in ICH patients [28]. Alternatively, remaining mutant type IV collagen present at BMs may also be nonfunctional or exert *de novo* deleterious effects.

Although molecular details of the mechanism underlying SMC degeneration remain unsettled, previous studies have shown that vascular BMs are important for SMC viability [29]. Notably, a polymorphism of the *COL4A2* gene that decreases the transcription of *COL4A1* and *COL4A2* has been shown to affect SMC survival [30]. Moreover, collagen type IV directly interacts with cellular receptors such as integrin $\beta1$, which plays a crucial role in SMC differentiation, contractile function, and survival [31,32]. Yet, it is unclear why SMC degeneration is focal and segmental, and occurs in a subset of arteries, especially in deep brain regions, whereas

COL4A1-COL4A2 expression is diffusely reduced in the cerebral vessels. One possibility may relate to the higher blood flow velocity and pulsatility in these deep brain arteries [33]. Of particular interest is the observation that ICHs associated with hypertension in humans affect the same deep brain regions [24]. Alternatively, there may be a threshold effect in the reduction of COL4A1-COL4A2 expression that could have gone undetected in our quantitative analyses.

Clinical management of COL4A1 or COL4A2 mutation carriers is especially challenging because only a small proportion of individuals will develop macroscopic hemorrhage in their lifetime. Recent work suggested that retinal imaging may be useful to identify patients at elevated risk of ICH [34]. In a cross-sectional analysis of a large cohort of heterozygous *Col4a1* G498V mice and a second cohort of homozygous mice displaying a more severe hemorrhagic phenotype, we discovered that imaging of the arterial wall in the retina is a promising tool for macroH risk stratification. Clinical translation of this approach should be straightforward since adaptive optics scanning laser ophthalmoscopy can noninvasively visualize morphological changes in mural cells of retinal arterioles and arteries in humans [19]. Such retinal biomarkers might be particularly useful for individual clinical management as well as for patient stratification or disease-activity monitoring in the context of clinical trials.

Collectively, our data support the concept that life-threatening macroH arise from SMC degeneration in a subset of arteries and suggest the possibility of identifying mutation carriers at high risk for macroscopic hemorrhage by assessing the arterial lesion load in the retina. Finally, our work identified "escaper" animals—*Col4a1* mutant mice that developed neither arterial lesions nor macroH despite a decreased expression of COL4A1/COL4A2. Used in conjunction with genome-wide sequencing and gene-expression profiling approaches, these mice represent an invaluable tool for identifying signaling pathways that protect against collagen deficiency, as recently exemplified in Duchene muscular dystrophy [35].

Acknowledgments

This work was supported by the Fondation Leducq (Transatlantic Network of Excellence on the Pathogenesis of Small Vessel Disease of the Brain), the European Union (Horizon 2020 Research and Innovation Programme SVDs@target under the grant agreement n° 666881), the French National Agency of Research (ANR I-Can), the French Fondation for Rare Diseases to AJ.

Author contributions

Study design and data interpretation, J.R. and A.J.; experiments, J.R., N.M., V.D. and A.R.; resources E.P.; writing, J.R. and A.J.; figures, J.R and N.M; supervision and funding acquisition, AJ.

References

1 Aguilar MI, Brott TG. Update in intracerebral hemorrhage. *The Neurohospitalist* 2011; **1**: 148-159

2 Rannikmäe K, Davies G, Thomson PA, *et al.* Common variation in COL4A1/COL4A2 is associated with sporadic cerebral small vessel disease. *Neurology* 2015; **84**: 918-926

3 Lanfranconi S, Markus HS. COL4A1 mutations as a monogenic cause of cerebral small vessel disease: a systematic review. *Stroke J Cereb Circ* 2010; **41**: e513-518

4 Vahedi K, Alamowitch S. Clinical spectrum of type IV collagen (COL4A1) mutations: a novel genetic multisystem disease. *Curr Opin Neurol* 2011; **24**: 63-68

5 Meuwissen MEC, Halley DJJ, Smit LS, *et al.* The expanding phenotype of COL4A1 and COL4A2 mutations: clinical data on 13 newly identified families and a review of the literature. *Genet Med Off J Am Coll Med Genet* 2015; **17**: 843-853

6 Khoshnoodi J, Pedchenko V, Hudson BG. Mammalian collagen IV. *Microsc Res Tech* 2008; **71**: 357-370

7 Jeanne M, Jorgensen J, Gould DB. Molecular and Genetic Analyses of Collagen Type IV Mutant Mouse Models of Spontaneous Intracerebral Hemorrhage Identify Mechanisms for Stroke Prevention. *Circulation* 2015; **131**: 1555-1565

8 Alamowitch S, Plaisier E, Favrole P, *et al.* Cerebrovascular disease related to COL4A1 mutations in HANAC syndrome. *Neurology* 2009; **73**: 1873-1882

9 Plaisier E, Gribouval O, Alamowitch S, *et al.* COL4A1 mutations and hereditary angiopathy, nephropathy, aneurysms, and muscle cramps. *N Engl J Med* 2007; **357**: 2687-2695

10 Chen Z, Migeon T, Verpont M-C, *et al.* HANAC Syndrome Col4a1 Mutation Causes Neonate Glomerular Hyperpermeability and Adult Glomerulocystic Kidney Disease. *J Am Soc Nephrol JASN* 2016; **27**: 1042-1054

11 Guiraud S, Migeon T, Ferry A, *et al.* HANAC Col4a1 Mutation in Mice Leads to Skeletal Muscle Alterations due to a Primary Vascular Defect. *Am J Pathol* 2017; **187**: 505-516

12 Trouillet A, Lorach H, Dubus E, *et al.* Col4a1 mutation generates vascular abnormalities correlated with neuronal damage in a mouse model of HANAC syndrome. *Neurobiol Dis* 2017; **100**: 52-61

13 Urabe N, Naito I, Saito K, *et al.* Basement membrane type IV collagen molecules in the choroid plexus, pia mater and capillaries in the mouse brain. *Arch Histol Cytol* 2002; **65**: 133-143

14 Hill RA, Tong L, Yuan P, *et al.* Regional Blood Flow in the Normal and Ischemic Brain Is Controlled by Arteriolar Smooth Muscle Cell Contractility and Not by Capillary Pericytes. *Neuron* 2015; **87**: 95-110

15 Tran KA, Zhang X, Predescu D, *et al.* Endothelial β-Catenin Signaling Is Required for Maintaining Adult Blood-Brain Barrier Integrity and Central Nervous System Homeostasis. *Circulation* 2016; **133**: 177-186

16 Yao Y, Chen Z-L, Norris EH, *et al.* Astrocytic laminin regulates pericyte differentiation and maintains blood brain barrier integrity. *Nat Commun* 2014; **5**: 3413

17 Zhao Z, Nelson AR, Betsholtz C, *et al.* Establishment and Dysfunction of the Blood-Brain Barrier. *Cell* 2015; **163**: 1064-1078

18 Patton N, Aslam T, Macgillivray T, *et al.* Retinal vascular image analysis as a potential screening tool for cerebrovascular disease: a rationale based on homology between cerebral and retinal microvasculatures. *J Anat* 2005; **206**: 319-348

19 Chui TYP, Gast TJ, Burns SA. Imaging of vascular wall fine structure in the human retina using adaptive optics scanning laser ophthalmoscopy. *Invest Ophthalmol Vis Sci* 2013; **54**: 7115-7124

20 Harb R, Whiteus C, Freitas C, *et al.* In vivo imaging of cerebral microvascular plasticity from birth to death. *J Cereb Blood Flow Metab Off J Int Soc Cereb Blood Flow Metab* 2013; **33**: 146-156

21 Auerbach ID, Sung SH, Wang Z, *et al.* Smooth muscle cells and the pathogenesis of cerebral microvascular disease ('angiomyopathies'). *Exp Mol Pathol* 2003; **74**: 148-159

22 Herzig MC, Winkler DT, Burgermeister P, *et al.* Abeta is targeted to the vasculature in a mouse model of hereditary cerebral hemorrhage with amyloidosis. *Nat Neurosci* 2004; **7**: 954-960

23 Schlunk F, Greenberg SM. The Pathophysiology of Intracerebral Hemorrhage Formation and Expansion. *Transl Stroke Res* 2015; **6**: 257-263

24 Sutherland GR, Auer RN. Primary intracerebral hemorrhage. *J Clin Neurosci Off J Neurosurg Soc Australas* 2006; **13**: 511-517

25 Haley KE, Greenberg SM, Gurol ME. Cerebral microbleeds and macrobleeds: should they influence our recommendations for antithrombotic therapies? *Curr Cardiol Rep* 2013; **15**: 425

26 Kuo DS, Labelle-Dumais C, Mao M, *et al.* Allelic heterogeneity contributes to variability in ocular dysgenesis, myopathy and brain malformations caused by Col4a1 and Col4a2 mutations. *Hum Mol Genet* 2014; **23**: 1709-1722

27 Jones FE, Bailey MA, Murray LS *et al*. ER stress and basement membrane defects combine to cause glomerular and tubular renal disease resulting from Col4a1 mutations in mice. *Dis Model Mech* 2016; **9**: 165-176

28 Lemmens R, Maugeri A, Niessen HWM, *et al.* Novel COL4A1 mutations cause cerebral small vessel disease by haploinsufficiency. *Hum Mol Genet* 2013; **22**: 391-397

29 Chen Z-L, Yao Y, Norris EH, *et al.* Ablation of astrocytic laminin impairs vascular smooth muscle cell function and leads to hemorrhagic stroke. *J Cell Biol* 2013; **202**: 381-395

30 Yang W, Ng FL, Chan K, *et al.* Coronary-Heart-Disease-Associated Genetic Variant at the COL4A1/COL4A2 Locus Affects COL4A1/COL4A2 Expression, Vascular Cell Survival, Atherosclerotic Plaque Stability and Risk of Myocardial Infarction. *PLoS Genet* 2016; **12**: e1006127

31 Abraham S, Kogata N, Fässler R, *et al.* Integrin beta1 subunit controls mural cell adhesion, spreading, and blood vessel wall stability. *Circ Res* 2008; **102**: 562-570

32 Turlo KA, Scapa J, Bagher P, *et al.* β1-integrin is essential for vasoregulation and smooth muscle survival in vivo. *Arterioscler Thromb Vasc Biol* 2013; **33**: 2325-2335

33 Bouvy WH, Geurts LJ, Kuijf HJ, *et al.* Assessment of blood flow velocity and pulsatility in cerebral perforating arteries with 7-T quantitative flow MRI. *NMR Biomed* 2016; **29**: 1295-1304

34 Alavi MV, Mao M, Pawlikowski BT, *et al*. Col4a1 mutations cause progressive retinal neovascular defects and retinopathy. *Sci Rep* 2016; **6**: 18602

35 Vieira NM, Elvers I, Alexander MS, *et al.* Jagged 1 Rescues the Duchenne Muscular Dystrophy Phenotype. *Cell* 2015; **163**: 1204-1213

Figure legends

Figure 1: *Col4a1* G498V mutant mice exhibit two distinct types of cerebral hemorrhages. (**A**) Representative images of sagittal brain sections from *Col4a1*$^{+/+}$ (+/+) mice and *Col4a1*$^{+/G498V}$ (+/G498V) mice, aged 1, 3 and 6 months, stained for hemosiderin. Bottom pictures show higher magnifications of boxed regions. Numerous fresh (black arrowhead) and old (white arrowhead) microh are seen at 1 month in mutant mice, and fewer macroH are detected at 3 and 6 months (arrow). (**B**) Representative images of consecutive brain sections from *Col4a1*$^{+/G498V}$ mice with microh (left row, 1 month) or macroH (right row, 3 months) stained for hemosiderin (Perls) (top) or CD68 (activated microglia/macrophages) and GFAP (reactive astrocytes) (bottom). (**C, D**) Quantification of the number of microh (**C**) and macroH (**D**) as defined in the method section (+/+, n = 16, 28 and 12 mice at 1, 3 and 6 months, respectively; +/G498V, n = 19, 24 and 45 mice at 1, 3 and 6 months, respectively). Significance was determined by Kruskal-Wallis test followed by Dunn's post hoc tests (**C**) and Fisher exact test (**D**) (*P < 0.05, ****P < 0.0001). Scale bars: 1 mm (**A**, top), 500 μm (**A**, bottom), and 100 μm (**B**).

Figure 2: Microh arise from transient leakage of capillaries. (**A**) Representative images of brain sections from 1-month-old *Col4a1*$^{+/G498V}$ (+/G498V) mice stained for α-SMA, perlecan, and hemoglobin (Hbα). RBCs in microh (arrowheads) are predominantly located around capillaries and to a lesser extent around post-capillary venules. (**B**) Quantification of the distribution of microh according to the parent vessel (n = 45 microh in 3 mice). (**C**) *Col4a1*$^{+/+}$ and *Col4a1*$^{+/G498V}$ mice, aged 1 or 3 months, were injected intraperitoneally with Evans blue. After allowing Evans blue to circulate for 16 hours, the brain was removed and nuclei were stained with DAPI. Representative images of whole sagittal brain sections showing diffuse leakage of Evans blue in *Col4a1*$^{+/G498V}$ mice at 1 month. Note that Evans blue fluorescence can

be observed in the choroid plexus (arrowhead) where endothelial cells are fenestrated. (**D**) Representative images of brain sections of *Col4a1*$^{+/+}$ and *Col4a1*$^{+/G498V}$ mice, aged 1 or 3 months, injected intravenously with FITC-albumin (FITC-Alb) (5 sections/mouse from 4 mice/group) and stained for the endothelial marker GLUT1 alone (top) or co-stained with GLUT1 and endogenous mouse IgGs (bottom). Diffuse extravasation of FITC-albumin and IgGs is seen in *Col4a1*$^{+/G498V}$ mice at 1 month. Scale bars: 50 μm (**A**, **D**) and 1 mm (**C**).

Figure 3: MacroH originate from arteries with impaired SMC coverage. (**A**) Representative images of a brain sample from a 3-month-old *Col4a1*$^{+/+}$ (+/+) mouse and from a *Col4a1*$^{+/G498V}$ (+/G498V) mouse with a fresh macroH, immunostained for α-SMA, perlecan and Hbα. Fresh macroH were identified beforehand by visual inspection of the brain sample. The bleeding vessel is characterized by robust deposition of Hbα within and outside its wall. Presence of α-SMA staining identifies this vessel as an artery. However discontinuous α-SMA staining in the bleeding vessel suggests focal loss of SMCs (yellow arrowheads). Three recent macroH from 3 different mutant mice were analyzed. (**B**) *Top panel*: Representative electron micrographs of a *Col4a1*$^{+/+}$ (+/+) mouse and hemorrhagic *Col4a1*$^{+/G498V}$ (+/G498V) arteries within the thalamus at 3 months of age. Asterisk shows a remaining SMC in the wall of the mutant artery. *Middle panel*: Higher magnification of boxed regions. *Bottom panel*: Schematic representations of the walls of control and hemorrhagic mutant arteries. Three different macroH from two *Col4a1*$^{+/G498V}$ mice were analyzed (4 sections per macroH). L, lumen; E, endothelium; SMC, smooth muscle cell; EBM, endothelial BM; SMBM, smooth muscle BM. Scale bars: 15 μm (**A**), 5 μm (**B**, top), 2 μm (**B**, bottom).

Figure 4: Focal and segmental SMC loss in cerebral arteries outside macroH. (**A**) Representative images of 100-μm-thick vibratome brain sections in a non-hemorrhagic area of

the brainstem from *Col4a1*$^{+/G498V}$ (+/G498V) mice at 3 months and from an age-matched *Col4a1*$^{+/+}$ (+/+) mouse, stained for α-SMA and perlecan, showing focal gaps in α-SMA labeling (arrowheads) in the mutant artery. Ten sections from five mice per group were analyzed. (**B, C**) *Top*: Representative electron micrographs of deep cerebral arteries from 3-month-old *Col4a1*$^{+/+}$ and *Col4a1*$^{+/G498V}$ mice outside a macroH showing SMC loss (**B**, arrows), SMCs with abnormal shape (**B**, asterisk), and abnormally thin SMCs (**C**, arrows) devoid of dense plaques (**C**, arrowheads in control artery) in *Col4a1*$^{+/G498V}$ mice. *Bottom:* Schematic representations of the walls of WT and mutant arteries. Eight ultra-thin sections from four different brain areas were analyzed in three *Col4a1*$^{+/+}$ and three *Col4a1*$^{+/G498V}$ mice. L, lumen; E, endothelium; SMC, smooth muscle cell; EBM, endothelial BM; SMBM, smooth muscle BM. Scale bars: 50 μm (**A**), 2 μm (**B**, **C**).

Figure 5: Progressive SMC loss in retinal arteries of *Col4a1* G498V mice. (**A**) Representative image of a flat-mounted retina stained for α-SMA (green) and perlecan (red). Arrowheads point to the proximal segment of a retinal artery. (**B**) Representative images of immunostaining for α-SMA and perlecan in proximal retinal arteries from *Col4a1*$^{+/+}$ (+/+) and *Col4a1*$^{+/G498V}$ (+/G498V) mice at the indicated ages. Arrowheads point to patchy gaps in α-SMA labeling in mutant mice by 3 months of age. (**C**) Quantification of SMC defects in the proximal segment of retinal arteries. Results are expressed as a percentage of the arterial bed containing patchy gaps in α-SMA labeling. From left to right: n = 13, 9, 11, and 8 mice. Significance was determined by Kruskal-Wallis test followed by Dunn's post hoc tests (***$P < 0.001$). (**D**) Representative images of co-immunostaining for PDGFRβ and α-SMA in the retinal arteries of *Col4a1*$^{+/+}$ and *Col4a1*$^{+/G498V}$ mice at 6 months; gaps in α-SMA labeling are not labeled by PDGFRβ antibody (arrowhead). Four control and 6 mutant mice were analyzed. (**E**) Representative images of immunostaining for cleaved caspase-3 (Cl-casp3) and α-SMA in

the retinal arteries of *Col4a1*$^{+/+}$ and *Col4a1*$^{+/G498V}$ mice at 6 months showing apoptotic cells (arrowheads) in the mutant artery. Yellow line delimitates the vessel. (**F**) Quantification of the percentage of the arterial bed containing cleaved capase-3–positive cells (n = 4 *Col4a1*$^{+/+}$ and 6 *Col4a1*$^{+/G498V}$ mice aged 6 months). Significance was determined by Student's t-test (*P < 0.05). Scale bars: 500 μm (**A**), 20 μm (**B**), 10 μm (**D**, **E**).

Figure 6: The severity of SMC loss in retinal arteries correlates with the macroH burden. (**A**) Representative images of immunostaining for α-SMA and perlecan in proximal retinal arteries from *Col4a1*$^{G498V/G498V}$ mice with macroH (macroH+) or without macroH (macroH-) at 3 months. (**B**) Quantification of SMC defects in the retinal arteries of *Col4a1*$^{G498V/G498V}$ mice with macroH (macroH+, n = 5 mice) or without macroH (macroH-, n = 9 mice) at 3 months. Significance was determined by Student's t-test (***P < 0.001). (**C**) Positive correlation (Spearman test) between the severity of SMC defects in retinal arteries and the number of macroH in 3-month-old *Col4a1*$^{G498V/G498V}$ mice. (**D**) Six-month-old *Col4a1*$^{+/G498V}$ mice (n = 45) were stratified into three groups according to the severity of SMC defects in retinal arteries: group I, 0.2% to 2.2% (n = 15 mice); group II, 2.3% to 7.8% (n = 15), and group III, 8.1% to 21.7% (n = 15). Bars represent the percentage of mice with macroH in each group. Scale bar: 20 μm.

Supporting information file contains supplementary methods and legend of supplementary Figures S1-9.

Supporting information

Severity of arterial defects in the retina correlates with the burden of intracerebral hemorrhage in COL4A1-related stroke

Julien Ratelade, Nicolas Mezouar, Valérie Domenga-Denier, Ambre Rochey, Emmanuelle Plaisier and Anne Joutel

Supplementary methods

Mouse genotyping

Mice were maintained in a specific pathogen-free environment. Genotyping analyses were performed by polymerase chain reaction (PCR) using the primer pair, 5'-TCC ATG TCC CCA AAG CCA TC-3' (forward) and 5'-GAA TTC CGC GCA GCT GAA AG-3' (reverse).

Immunohistochemistry and antibodies

Mice were transcardially perfused with PBS and the brain was removed. The left cerebral hemisphere was flash-frozen for cryosectioning, and the right hemisphere was fixed in 4% PFA overnight and cut into 100-µm-thick sagittal sections using a vibratome. Acetone-fixed cryosections (10-µm-thick) or vibratome sections (100-µm-thick) were blocked in 5% bovine serum albumin (BSA) for 1 hour at room temperature. Sections were then incubated overnight at 4°C with primary antibodies diluted in PBS containing 0.5% BSA (PBS/0.5% BSA) and with secondary antibodies diluted in PBS/0.5% BSA for 3 hours at room temperature. Stained sections were imaged with an Eclipse 80i microscope (Nikon, Champigny sur Marne, France). Sections immunostained for COL4A1 or COL4A2 were imaged at the ImagoSeine facility (Institut Jacques Monod, Paris, France) with a TCS SP5 laser-scanning confocal

microscope (Leica Microsystems, Nanterre, France).

The indicated primary antibodies to the following proteins were used: CD68 (1/500, clone FA-11; Bio-Rad, Oxford, UK), GFAP (1/1000; Sigma Aldrich, St. Louis, MO, USA), hemoglobin α (1/500; Santa Cruz Biotechnology, Santa Cruz, CA, USA), perlecan (1/1000, clone A7L6; Millipore, Temecula, CA, USA), biotinylated perlecan (1/1000, clone A7L6; Abcam, Cambridge, UK), α-SMA (1/1000, clone 1A4; Abcam [Alexa Fluor 594-conjugated] or Sigma Aldrich [FITC-conjugated]), COL4A1 and COL4A2 NC1 domains (1/200, clones H11 and H22; Chondrex Inc., Redmond, WA, USA), COL4A3 and COL4A6 NC1 domains (1/200, clone H31 and M69; from Dr Y. Sado, Shigei Medical Research Institute, Okayama, Japan), elastin (1/500; from Dr. R. Mecham, Washington University School of Medicine, St. Louis, MO, USA), GLUT1 (1/1000; Millipore), PDGFRβ (1/500, clone APB5; eBiosciences, San Diego, CA, USA), and cleaved caspase-3 (1/500; Cell Signaling Technology, Danvers, MA, USA). Alexa Fluor-488–, Alexa Fluor-594– or Alexa Fluor-647–conjugated secondary antibodies were used (1/500; Life Technologies, Saint-Aubin, France).

Flat-mounted retinas

Eyes were removed and fixed in 4% PFA for 2 hours at 4°C. Retinas were then dissected under a microscope and processed for immunostaining using the protocol described above.

Blood-brain barrier (BBB) permeability

Mice were injected intravenously in the tail vein with 82.5 mg/kg FITC-albumin (Sigma Aldrich) or intraperitoneally with 2% Evans blue (10 μL/g). After 16 hours, mice were anesthetized and perfused with PBS, after which their brains were fixed in 4% PFA overnight. For FITC-albumin visualization, brains were processed for cryopreservation, and free-floating 16-μm-thick sections were then immunostained for the endothelial marker GLUT1 and

endogenous mouse immunoglobulins as described above. For Evans blue visualization, brains were cut into 100-µm-thick sagittal sections, and nuclei were stained with 4′,6-diamidine-2′-phenylindole dihydrochloride (DAPI).

RNA preparation and quantitative reverse transcription-polymerase chain reaction (qRT-PCR) analyses

Cerebral microvessels, isolated from frozen brains as described previously [1], were homogenized on ice in SV RNA lysis buffer (Promega, Madison, WI, USA) using a polytron homogenizer, and total RNA was extracted following the manufacturer's protocol (SV Total RNA Isolation System; Promega). cDNA was synthesized from total RNA using M-MLV reverse transcriptase (ThermoFisher Scientific, Waltham, MA, USA). RT-qPCR was performed on a CFX Connect Real-Time PCR detection system (Bio-Rad, Oxford, UK) using SYBR Green PCR master mix (Bio-Rad). The following primer pairs were used: *β-actin*, 5'-CTG CGT CTG GAC CTG GCT-3' (forward) and 5'-ACG CAC GAT TTC CCT CTC A-3' (reverse); *sXBP1*, 5'-CTG AGT CCG CAG CAG GTG-3' (forward) and 5'-ACA GGG TCC AAC TTG TCC AG-3' (reverse); *Hspa5* (GRP78), 5'-CCG AGT GAC AGC TGA AGA CA-3' (forward) and 5'-GCG CTC TTT GAG CTT TTT GT-3' (reverse); and *Ddit3* (CHOP), 5'-CAG AGT TCT ATG GCC CAG GA-3' (forward) and 5'-CTG CTC CTT CTC CTT CAT GC-3' (reverse). Results are presented as β-actin–normalized relative expression levels.

Quantitative analysis

All quantifications were performed using ImageJ (https://imagej.nih.gov/ij/) and all procedures were performed with prefixed parameters under blinded conditions.

Intracerebral hemorrhages. Microhemorrhages and macrohemorrhages, including both fresh and old hemorrhages, were counted on Perl's-stained brain sections using a custom-made

macro. Surfaces of bleeds were determined on brain sections, and their diameter was estimated by considering the surface as a disk. A cut-off diameter of 150 µm was used to categorize micro- and macrohemorrhages. Twelve 50-µm-thick sections, spaced 150 µm apart and spanning an entire hemisphere (Figures 1, 6B, C and S1), and 24 sections, spaced 150 µm apart and spanning the entire brain (Figure 6D), were analyzed per mouse.

COL4A1/2/6 staining. Quantification was performed on 10-µm-thick brain cryosections labeled for COL4A1, COL4A2 or COL4A6 together with perlecan and α-SMA. Epifluorescence images (416×351 µm^2) were obtained from the thalamus and brainstem (where most of the cerebral bleeds were observed). The mean signal intensity of COL4A1 and COL4A2 staining was measured in capillaries (vessels with a diameter ranging from 3 to 9 µm positive for perlecan and negative for α-SMA) and arteries (vessels positive for perlecan and α-SMA) (n = 5–8 images/mouse). Mean signal intensity of COL4A6 was quantified in arteries (n = 5–8 images/mouse).

Scoring smooth muscle cell defects. Quantification was performed on flat-mounted retinas labeled for α-SMA and perlecan. Epifluorescence images were obtained from the whole retina, and arterial segments within a 1.5-mm radius centered on the optic nerve were visually inspected for gaps in α-SMA labeling. The length of arterial segments with gaps as well as the total length of arterial segments were measured (1 retina/mouse). Results are expressed as the percentage of the arterial bed containing gaps.

Cleaved caspase-3 staining. Quantification was performed on flat-mounted retinas labeled for α-SMA and cleaved caspase-3. Results are expressed as the percentage of the arterial bed positive for the cleaved caspase-3 marker over total arterial length (1 retina/mouse).

Pericyte coverage. Quantification was performed on 10-µm-thick brain cryosections labeled for PDGFRβ and perlecan. Epifluorescence images (416×351 µm^2) were obtained from the thalamus and brainstem (where most of the extravasation of fluorescent tracers was

observed), and areas stained for PDGFRβ and perlecan were measured. Pericyte coverage is reported as the percentage of PDGFRβ-stained area over perlecan-stained area.

Transmission electron microscopy

Mice were transcardially perfused first with PBS and then with 2% PFA. The brain was removed and cut into 1-mm^3 blocks. Blocks were incubated overnight in 2% glutaraldehyde/2% PFA, post-fixed in 2% osmium tetroxide, dehydrated by passage through a graded series of ethanol concentrations, and embedded in epoxy resin. Semi-thin sections (1 µm) were prepared, stained with toluidine blue, and examined by light microscopy using a Leica DMR microscope (Leica Microsystems) to select regions of interest within or outside macroscopic hemorrhages. Ultra-thin sections (75 nm thick) of a region of interest were cut, contrasted with uranyl acetate and lead citrate, and examined by transmission electron microscopy (Philips CM100) at Institut du Fer à Moulin (Paris, France).

Supplementary reference

[1] Monet-Leprêtre M, Haddad I, Baron-Menguy C, Fouillot-Panchal M, Riani M, Domenga-Denier V, Dussaule C, Cognat E, Vinh J, Joutel A (2013) Abnormal recruitment of extracellular matrix proteins by excess Notch3 ECD: a new pathomechanism in CADASIL. Brain J Neurol 136:1830–1845. doi: 10.1093/brain/awt092

Supplementary figure legend

Figure S1: Micro and macrohemorrhages in *Col4a1*$^{G498V/G498V}$ mice. (A) Representative images of sagittal brain sections from *Col4a1*$^{+/+}$ (+/+) mice and *Col4a1*$^{G498V/G498V}$ (G498V/G498V) mice, aged 1 and 3 months, stained for hemosiderin. Bottom pictures show

higher magnifications of boxed regions. Numerous fresh (black arrowhead) and old (white arrowhead) microh are seen at 1 month in mutant mice, and a few macroH are detected at 3 months (arrow). (**B, C**) Quantification of the number of microh (**B**) and macroH (**C**) as defined in the method section (+/+, n = 10 and 14 mice at 1 and 3 months, respectively; G498V/G498V, n = 9 and 14 mice at 1 and 3 months, respectively). Significance was determined by Kruskal-Wallis test followed by Dunn's post hoc tests (**B**) and Fisher exact test (**C**) (**P* < 0.05, ****P* < 0.001, *****P* < 0.0001). Scale bars: 1 mm (**A**, top), 500 μm (**A**, bottom).

Figure S2: Structural abnormalities of vascular BMs in *Col4a1* G498V mutant mice. Representative electron micrographs of a brain capillary wall (**A**) and a brain arterial wall (**B**) from 3-month-old *Col4a1*$^{+/+}$ (+/+) and *Col4a1*$^{+/G498V}$ (+/G498V) mice. Black arrowheads delimitate the endothelial BM in capillaries (**A**) and the smooth muscle BM in arteries (**B**). Asterisk points to a focal interruption of the BM. BMs are thinner with fuzzy edges in mutant mice compared to controls. Eight ultra-thin sections from four different brain areas were analyzed in three *Col4a1*$^{+/+}$ and three *Col4a1*$^{+/G498V}$ mice. L, lumen; E, endothelial cell; SMC, smooth muscle cell. Scale bars: 250 nm (**A**), 500 nm (**B**).

Figure S3: Cerebral vessels of *Col4a1* G498V mutant mice exhibit reduced BM levels of COL4A1 and COL4A2 but no intracellular accumulation. (**A**) Representative images of immunostaining for COL4A1 (top) and perlecan/α-SMA (bottom) in the adult brain from *Col4a1*$^{+/+}$ (+/+), *Col4a1*$^{+/G498V}$ (+/G498V) and *Col4a1*$^{G498V/G498V}$ (G498V/G498V) mice, showing less intense COL4A1 labeling in mutant mice. Arrowheads point to arteries. (**B**) Representative confocal microscopy images (5 sections/mouse from 4 mice/group) of capillaries from wild-type and G498V mutant mice immunostained for COL4A1 and perlecan

showing uniform distribution of COL4A1, but with reduced immunofluorescence intensity, at endothelial-pericyte BMs in *Col4a1*$^{+/G498V}$ and *Col4a1*$^{G498V/G498V}$ capillaries, with no evidence of intracellular accumulation. (**C**) Representative confocal microscopy images (5 sections/mouse from 4 mice/group) of arteries from wild-type and G498V mutant mice immunostained for COL4A1, perlecan and α-SMA showing uniform distribution of COL4A1 at smooth muscle BMs in *Col4a1*$^{+/G498V}$ and *Col4a1*$^{G498V/G498V}$ arteries, with no evidence of intracellular accumulation. Yellow arrowheads point to smooth muscle BMs intercalated between SMCs. (**D**) Quantification of the fluorescence intensity of COL4A1 (n = 4 mice/group) in cerebral capillaries and arteries. (**E**) Representative images of immunostaining for COL4A2 (top) and perlecan/α-SMA (bottom) in the adult brain from *Col4a1*$^{+/+}$, *Col4a1*$^{+/G498V}$ and *Col4a1*$^{G498V/G498V}$ mice, showing a strong reduction in COL4A2 labeling in mutant mice. Arrowheads point to arteries. (**F**) Quantification of the fluorescence intensity of COL4A2 (n = 4 mice/group) in cerebral capillaries and arteries. Significance was determined by one-way ANOVA followed by Tukey's post hoc tests (*$P < 0.05$; **$P < 0.01$; ****$P < 0.0001$). Scale bars: 50 μm (**A**, **E**), 10 μm (**B, C**).

Figure S4: No increased expression of ER-stress markers in *Col4a1* G498V cerebral microvessels. Assessment of relative mRNA expression levels of the endoplasmic reticulum stress-induced genes coding for C/EBP homologous protein (CHOP), glucose-regulated protein 78 (GRP78) and X-box–binding protein 1 spliced (sXBP1) in brain microvessels isolated from adult *Col4a1*$^{+/+}$ (+/+) and *Col4a1*$^{+/G498V}$ (+/G498V) mice. (n = 6 biological replicates/group, each biological replicate prepared from 2 mice). No statistical difference was found between *Col4a1*$^{+/+}$ and *Col4a1*$^{+/G498V}$ mice.

Figure S5: Expression of COL4A3 and COL4A6 is unchanged in brain vessels of *Col4a1* G498V mutant mice. (**A**) Representative images of immunostaining for COL4A3 (top) and perlecan/α-SMA (bottom) in the adult brain from *Col4a1*$^{+/+}$ (+/+) and *Col4a1*$^{+/G498V}$ (+/G498V) mice, showing COL4A3 expression in choroid plexus (Cp) but no staining in cerebral vessels. (B) Representative images of immunostaining for COL4A6 (top) and perlecan/α-SMA (bottom) showing COL4A6 expression only in arteries of *Col4a1*$^{+/+}$ mice and comparable expression in *Col4a1*$^{+/G498V}$ mice. Arrowheads point to arteries. (C) Quantification of the fluorescence intensity of COL4A6 in arteries (n = 4 mice/group). Significance was determined by Student's t-test (ns: not significant). Scale bar: 50 μm.

Figure S6: Transient increase in BBB permeability in *Col4a1*$^{G498V/G498V}$ mice. *Col4a1*$^{+/+}$ and *Col4a1*$^{G498V/G498V}$ mice, aged 1 or 3 months (n = 3 mice per group), were injected intraperitoneally with Evans blue. After allowing Evans blue to circulate for 16 hours, the brain was removed and nuclei were stained with DAPI. Representative images of whole sagittal brain sections showing diffuse leakage of Evans blue in *Col4a1*$^{G498V/G498V}$ mice at 1 month. Arrowhead point to Evans blue extravasation in choroid plexus where endothelial cells are fenestrated. Scale bar: 1 mm.

Figure S7: Pericyte coverage of capillaries is unaffected in *Col4a1* G498V mutant mice. **(**A) Representative images of immunostaining for PDGFRβ and perlecan in the brain of young *Col4a1*$^{+/+}$ (+/+) and *Col4a1*$^{+/G498V}$ (+/G498V) mice. (B) Quantification of the pericyte coverage in cerebral capillaries of *Col4a1*$^{+/+}$ and *Col4a1*$^{+/G498V}$ mice (n = 6 mice/group). Significance was determined by Student's t-test (ns: not significant). Scale bar: 50 μm.

Figure S8: MacroH originate from arteries with SMC loss in *Col4a1*$^{G498V/G498V}$ mice. *Top panel*: Representative images of a brain sample from a 3-month-old *Col4a1*$^{+/+}$ (+/+) mouse and a fresh macroH from a *Col4a1*$^{G498V/G498V}$ (G498V/G498V) mouse immunostained for α-SMA and mouse IgGs, and counterstained with DAPI. Fresh macroH, identified beforehand by visual inspection of the brain sample, were visualized by light microscopy and epifluorescence microscopy as regions with a lower density of nucleated cells (yellow line). The bleeding vessel is characterized by robust deposition of endogenous IgG within and around its wall (white arrowheads, right panel). *Middle and bottom panel*: Higher magnification view of vessels depicted by white arrowheads in top panel and stained for α-SMA and elastin. Shown is focal loss of SMCs (yellow arrowheads), and some remaining SMCs (white arrow), with focal rupture of the elastic lamina (blue arrowheads) in the mutant hemorrhagic artery. Five recent macroH from four different mutant mice were analyzed. Scale bars: 100 μm (top), 25 μm (bottom).

Figure S9: SMC loss in retinal arteries of *Col4a1*$^{G498V/G498V}$ mice. (**A**) Representative images of immunostaining for α-SMA and perlecan in proximal retinal arteries from *Col4a1*$^{+/+}$ (+/+) and *Col4a1*$^{G498V/G498V}$ (G498V/G498V) mice at 3 months. Arrowheads point to patchy gaps in α-SMA labeling in mutant mice. (**B**) Quantification of SMC defects in the proximal segment of retinal arteries in *Col4a1*$^{+/G498V}$ and *Col4a1*$^{G498V/G498V}$ mice at 3 months (n = 11 and 14 mice). Significance was determined by Mann-Whitney test (**$P < 0.01$). (**C**) Representative images of immunostaining for α-SMA and DAPI in retinal arteries of *Col4a1*$^{+/+}$ and *Col4a1*$^{G498V/G498V}$ mice at 3 months. White dashed lines delimitate the vessels. Yellow lines delimitate areas with absence of α-SMA staining. Yellow asterisks point to nuclei of endothelial cells (elongated and oriented toward the vessel axis); white open circles point to SMC nuclei (more rounded and perpendicular to the vessel axis). Areas with loss of

α-SMA staining do not contain SMC nuclei suggesting loss of SMCs in mutant arteries. (**D**) Representative images of co-immunostaining for PDGFRβ and α-SMA in the retinal arteries of *Col4a1*$^{+/+}$ and *Col4a1*$^{G498V/G498V}$ mice at 3 months; gaps in α-SMA labeling are not labeled by PDGFRβ antibody (arrowhead). Five mice per group were analyzed. (**E**) Representative images of immunostaining for cleaved caspase-3 (Cl-casp3) and α-SMA in the retinal arteries of *Col4a1*$^{+/+}$ and *Col4a1*$^{G498V/G498V}$ mice at 3 months showing apoptotic cells in the mutant artery. (**F**) Quantification of the percentage of the arterial bed containing cleaved capase-3–positive cells (n = 5 mice/group). Significance was determined by Student's t-test (**$P < 0.01$). Scale bar: 10 μm.

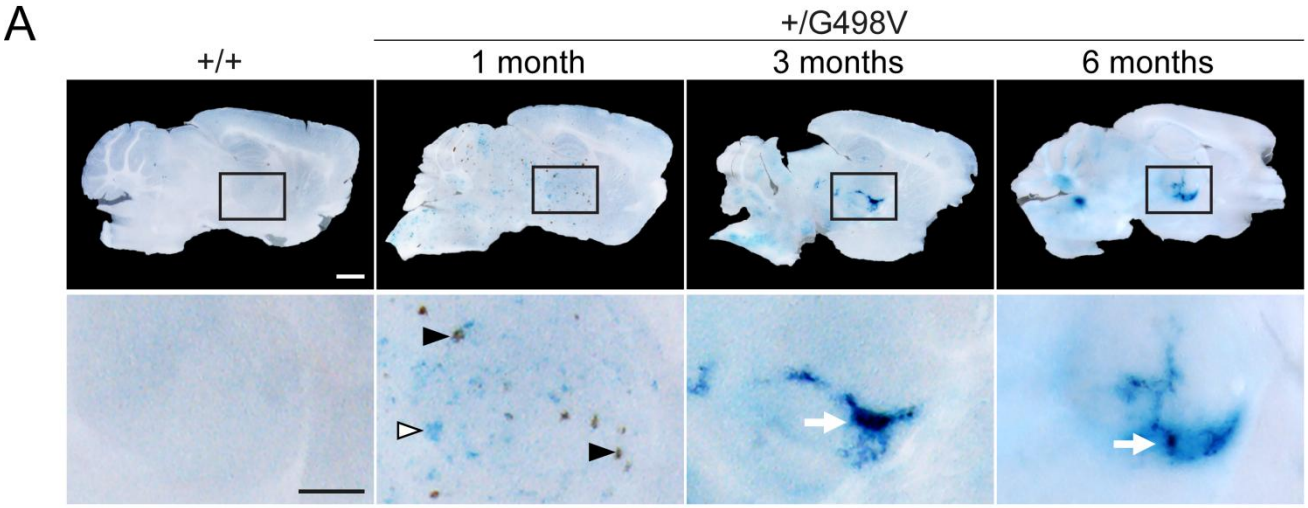
A
+/+
+/G498V
1 month
3 months
6 months

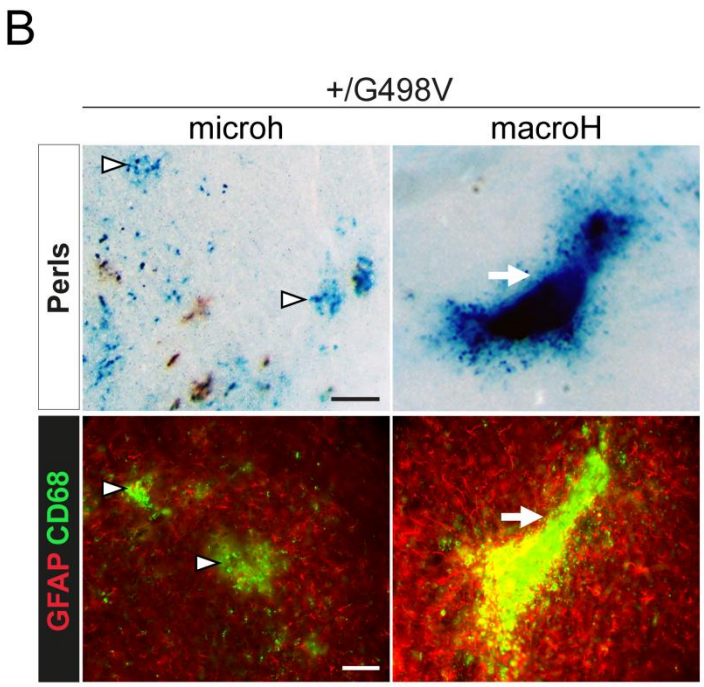
B
+/G498V
microh
macroH
Perls
GFAP CD68

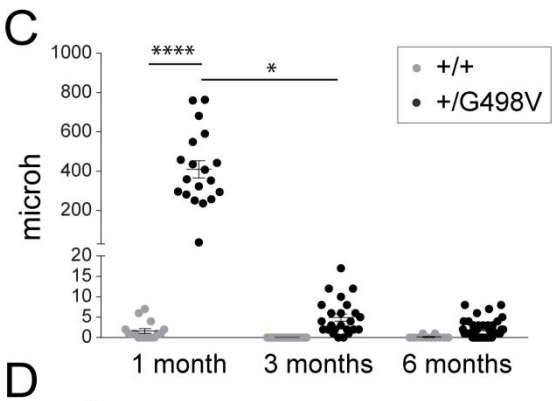
C
****
*
+/+
+/G498V
microh
1000
800
600
400
200
20
15
10
5
0
1 month
3 months
6 months

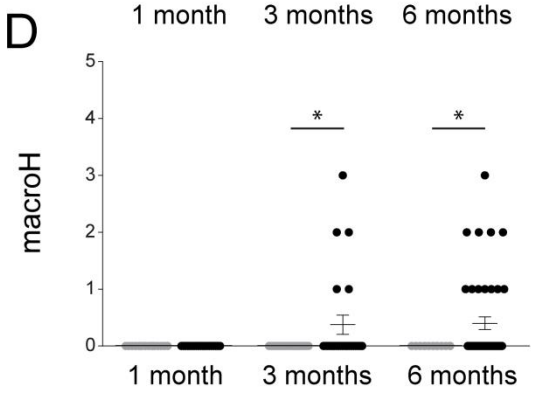
D
*
*
macroH
5
4
3
2
1
0
1 month
3 months
6 months

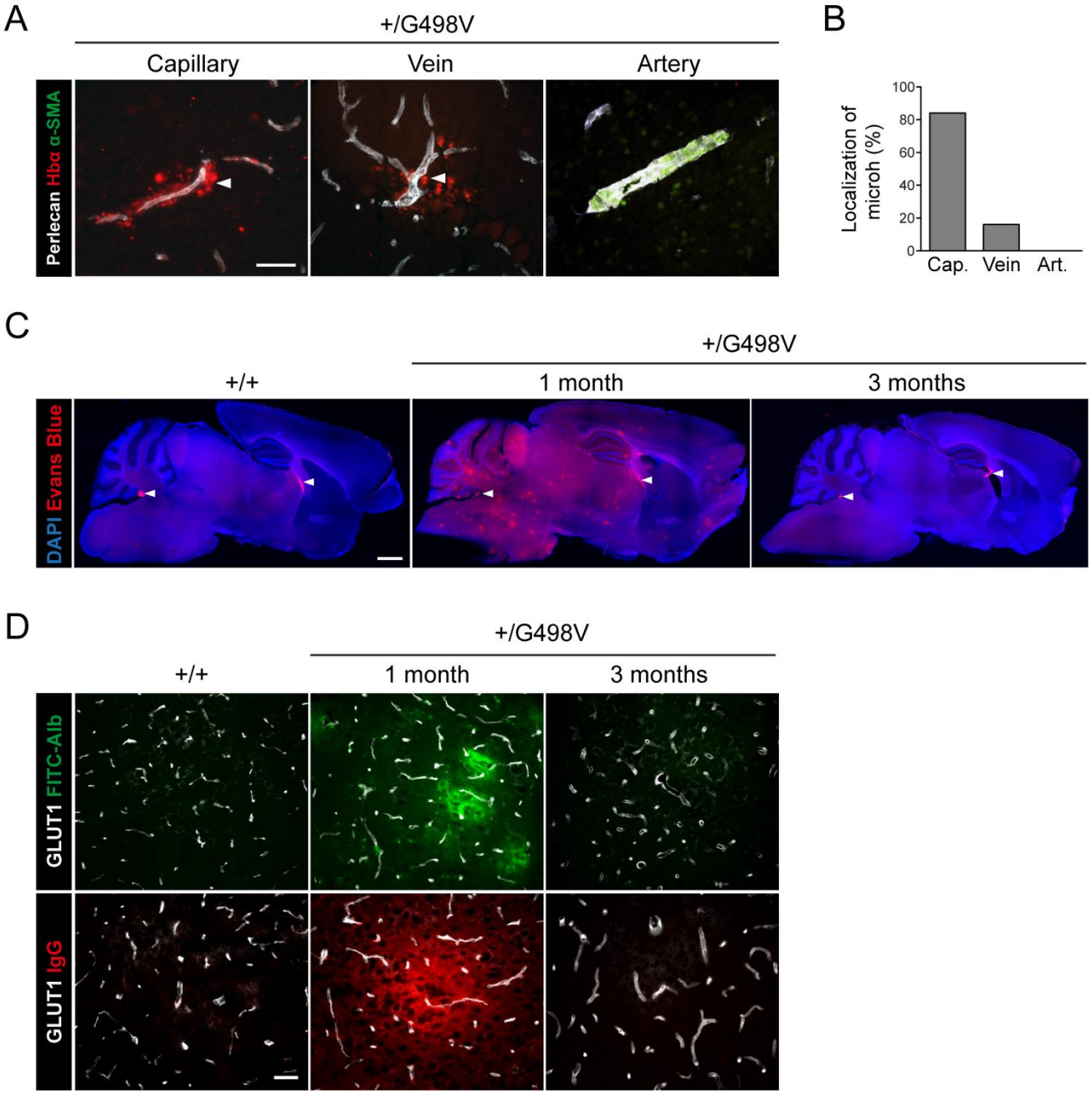
A
+/G498V
Capillary
Vein
Artery
Perlecan Hbα α-SMA
B
Localization of microh (%)
100
80
60
40
20
0
Cap.
Vein
Art.
C
+/G498V
+/+
1 month
3 months
DAPI Evans Blue
D
+/G498V
+/+
1 month
3 months
GLUT1 FITC-Alb
GLUT1 IgG

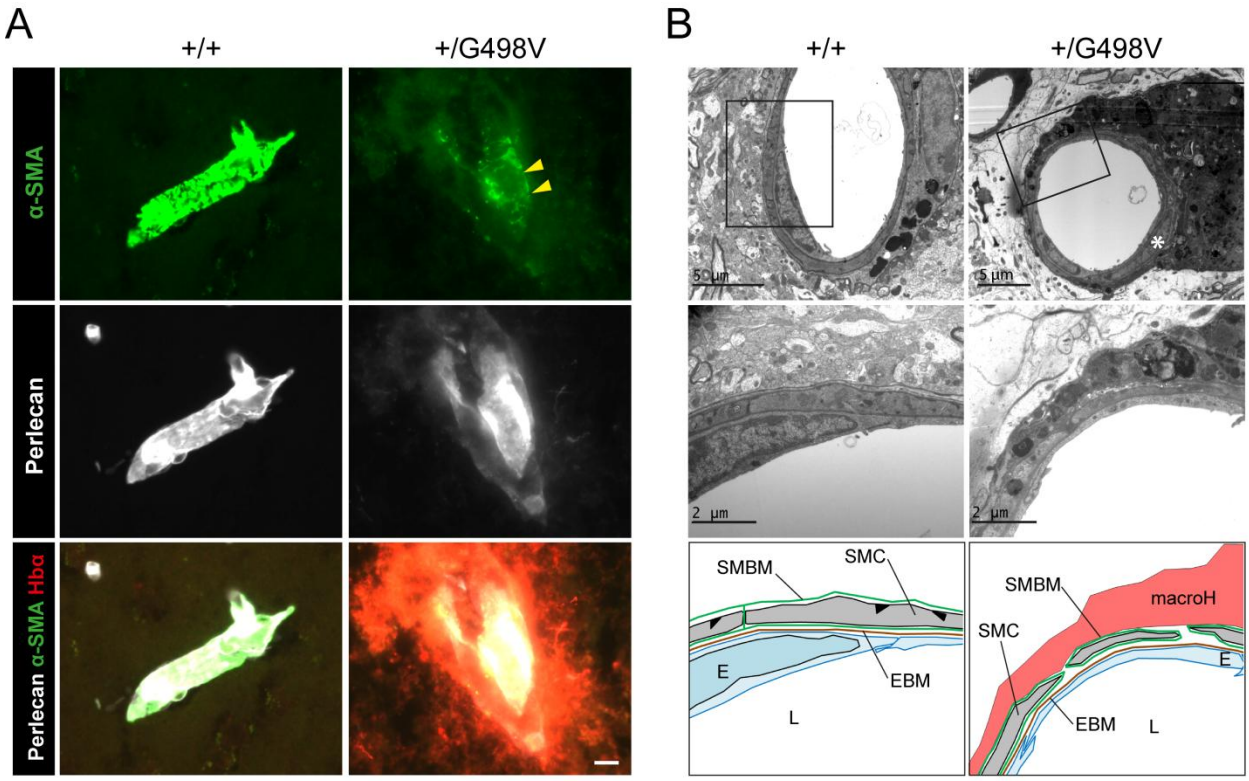
A
+/+
+/G498V
α-SMA
Perlecan
Perlecan α-SMA Hbα
B
+/+
+/G498V
5 µm
5 µm
2 µm
2 µm
SMBM
SMC
E
EBM
L
SMBM
macroH
SMC
E
EBM
L

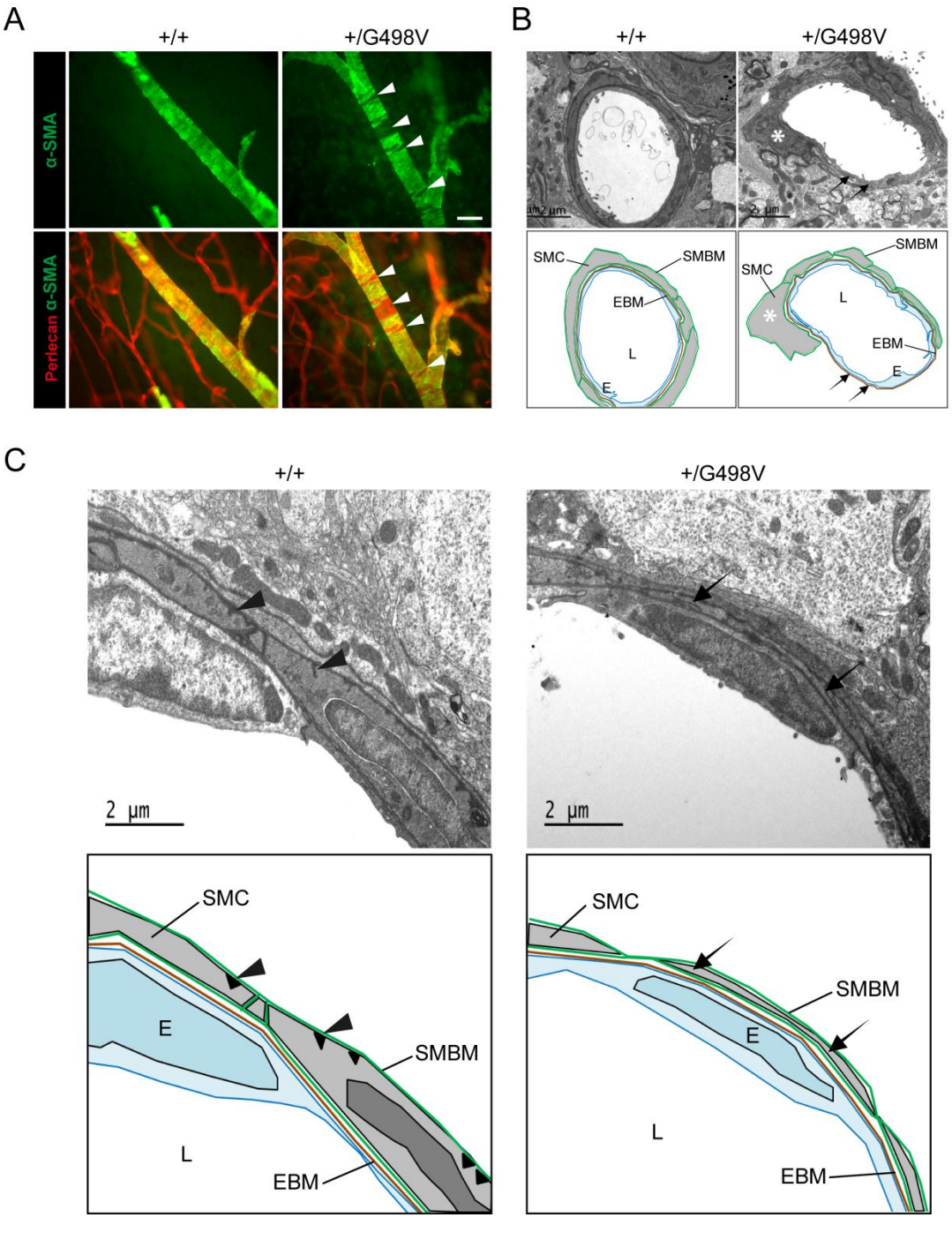
A
+/+
+/G498V
α-SMA
Perlecan α-SMA
B
+/+
+/G498V
SMC
SMBM
EBM
L
E
C
+/+
+/G498V
2 µm
SMC
SMBM
E
L
EBM

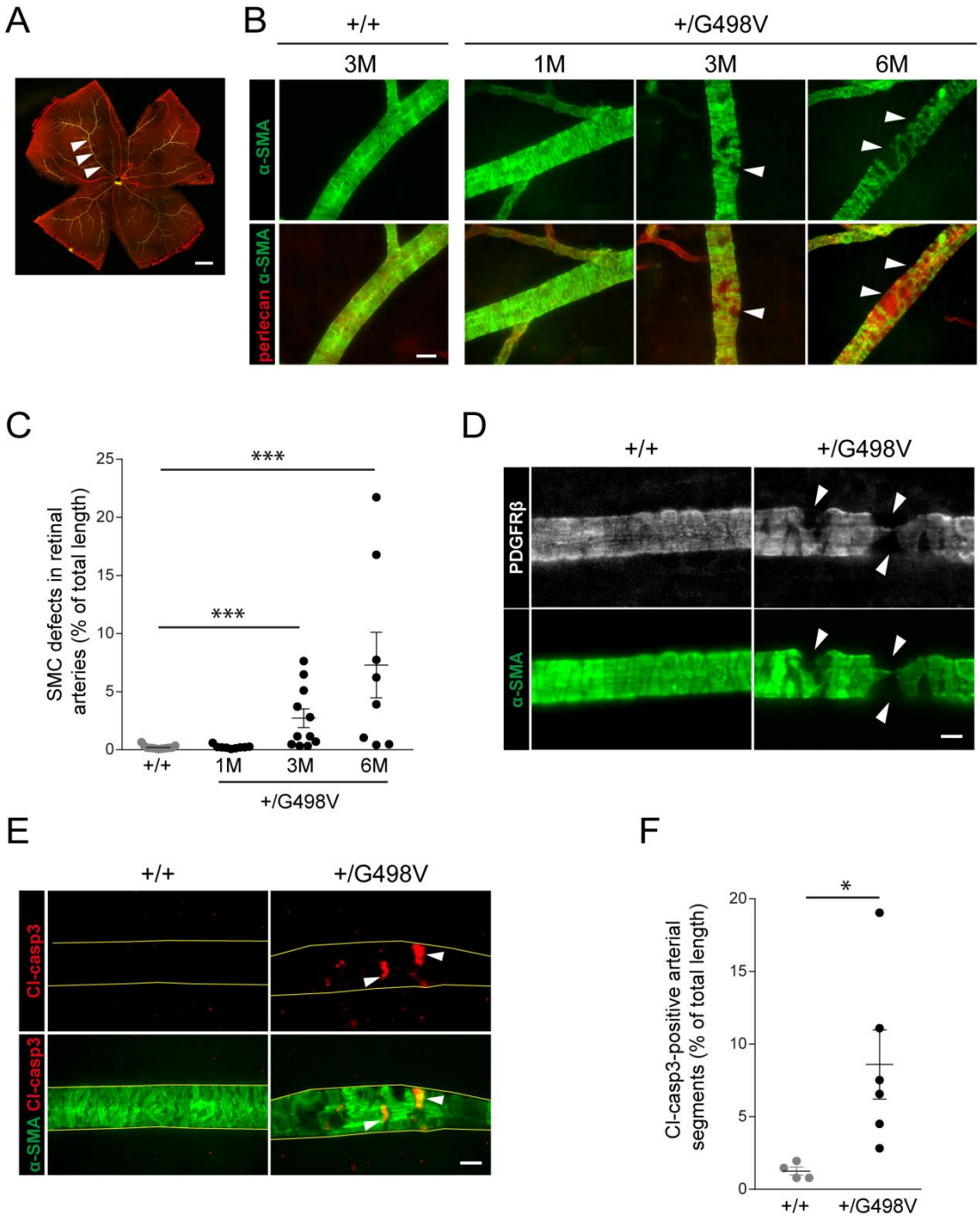
A
B
+/+
+/G498V
3M
1M
3M
6M
α-SMA
perlecan α-SMA
C
SMC defects in retinal arteries (% of total length)
***
***
+/+
1M
3M
6M
+/G498V
D
+/+
+/G498V
PDGFRβ
α-SMA
E
+/+
+/G498V
Cl-casp3
α-SMA Cl-casp3
F
Cl-casp3-positive arterial segments (% of total length)
*
+/+
+/G498V

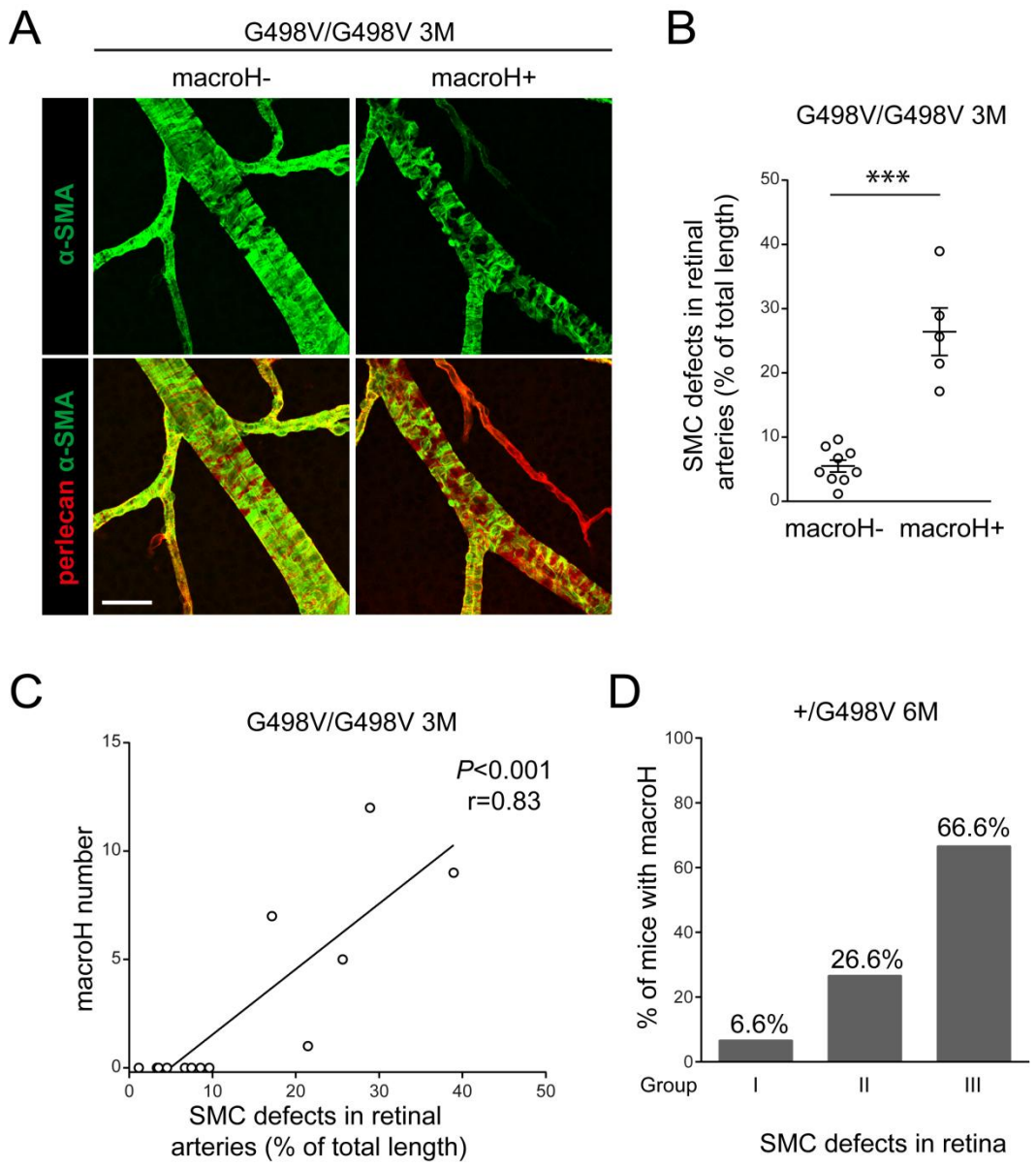
A
G498V/G498V 3M
macroH-
macroH+
α-SMA
perlecan α-SMA
B
G498V/G498V 3M
***
SMC defects in retinal arteries (% of total length)
50
40
30
20
10
0
macroH-
macroH+
C
G498V/G498V 3M
P<0.001
r=0.83
macroH number
15
10
5
0
0
10
20
30
40
50
SMC defects in retinal arteries (% of total length)
D
+/G498V 6M
% of mice with macroH
100
80
60
40
20
0
6.6%
26.6%
66.6%
Group
I
II
III
SMC defects in retina

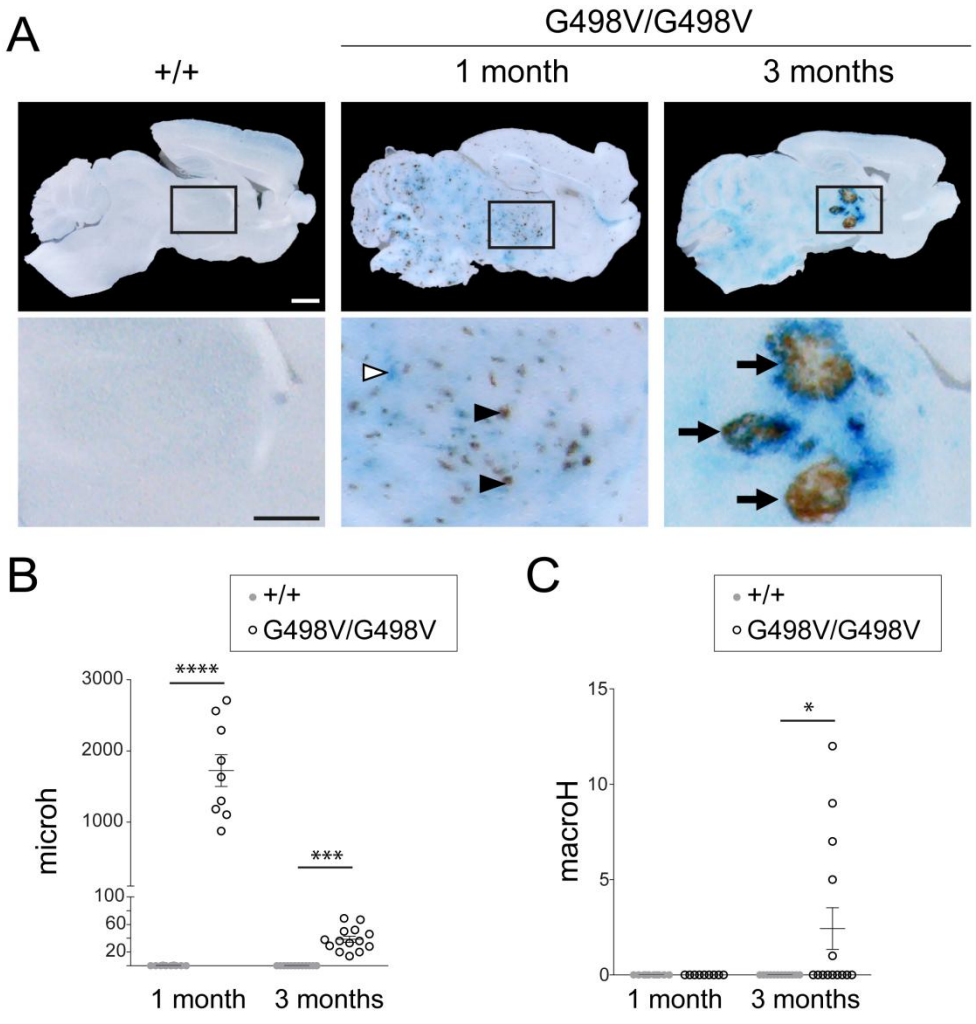
A
G498V/G498V
+/+
1 month
3 months
B
+/+
G498V/G498V
microh
3000
2000
1000
100
60
20
****
***
1 month
3 months
C
+/+
G498V/G498V
macroH
15
10
5
0
*
1 month
3 months

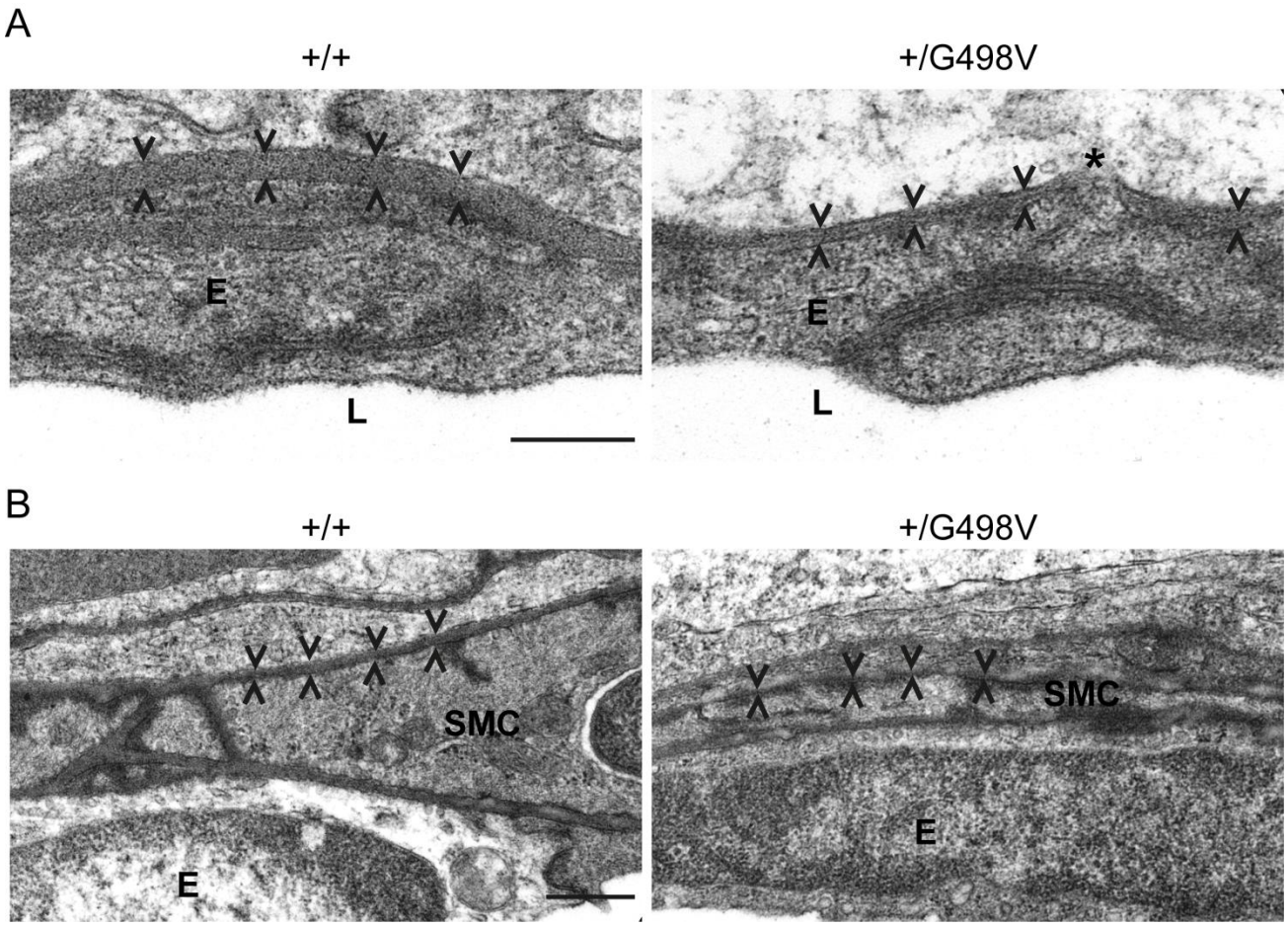
A
+/+
+/G498V
E
L
*
B
+/+
+/G498V
SMC
E
SMC
E

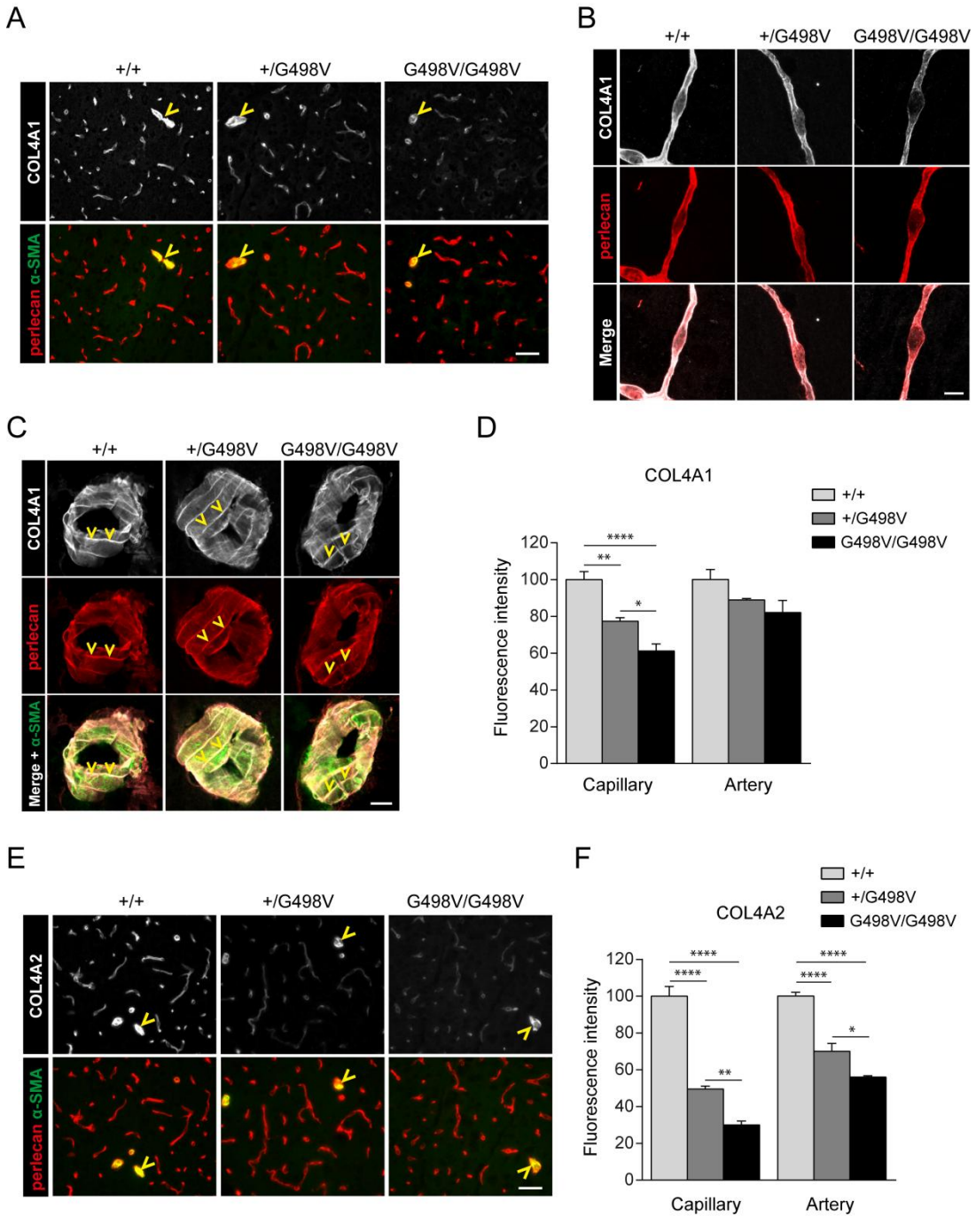
A
+/+
+/G498V
G498V/G498V
COL4A1
perlecan α-SMA
B
+/+
+/G498V
G498V/G498V
COL4A1
perlecan
Merge
C
+/+
+/G498V
G498V/G498V
COL4A1
perlecan
Merge + α-SMA
D
COL4A1
+/+
+/G498V
G498V/G498V
Fluorescence intensity
120
100
80
60
40
20
0
****
**
*
Capillary
Artery
E
+/+
+/G498V
G498V/G498V
COL4A2
perlecan α-SMA
F
COL4A2
+/+
+/G498V
G498V/G498V
Fluorescence intensity
120
100
80
60
40
20
0
****
****
****
****
**
*
Capillary
Artery

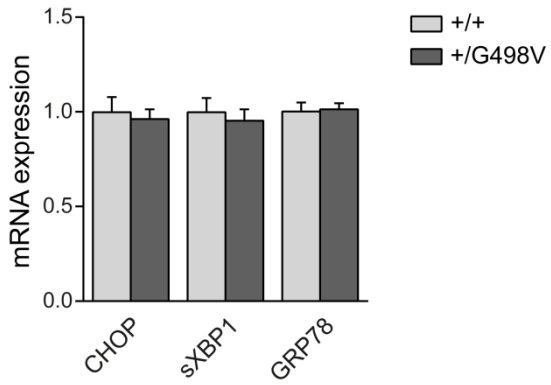
1.5
1.0
0.5
0.0
mRNA expression
+/+
+/G498V
CHOP
sXBP1
GRP78

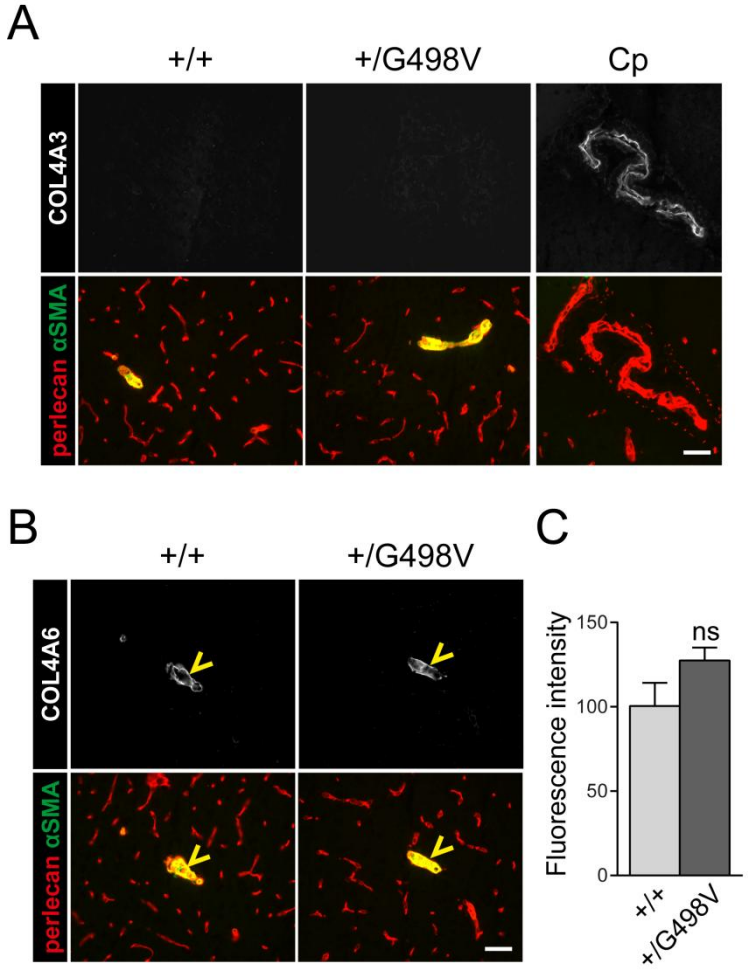
A
+/+
+/G498V
Cp
COL4A3
perlecan αSMA
B
+/+
+/G498V
COL4A6
perlecan αSMA
C
Fluorescence intensity
150
100
50
0
ns
+/+
+/G498V

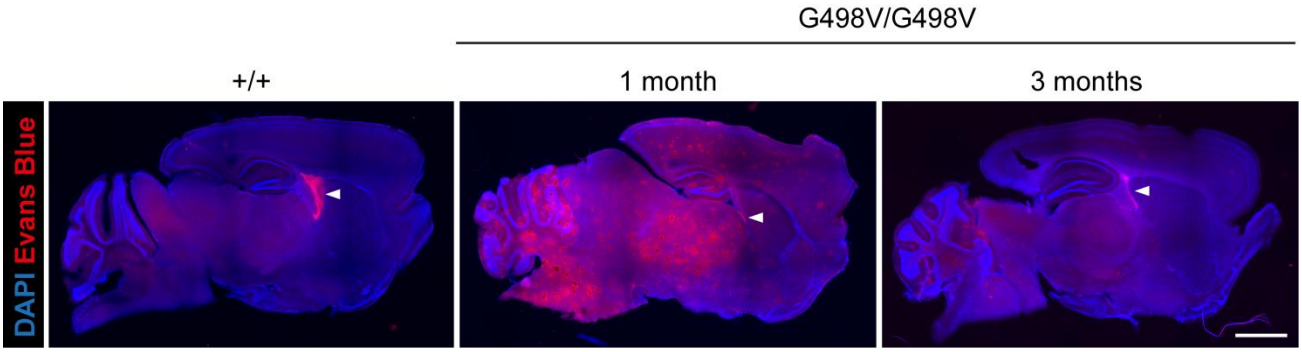
G498V/G498V
+/+
1 month
3 months
DAPI Evans Blue

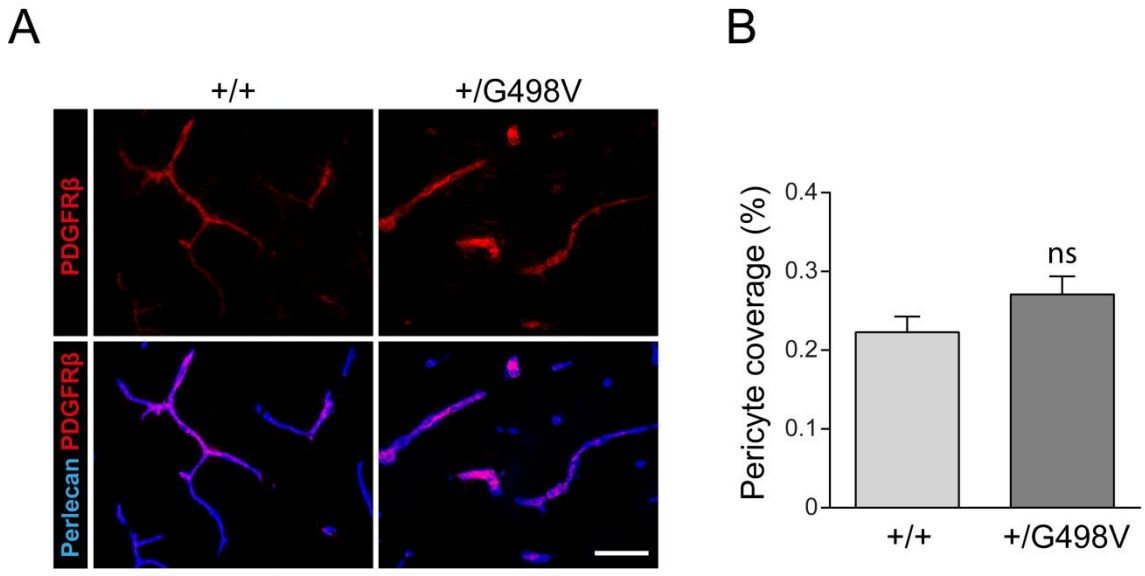
A
+/+
+/G498V
PDGFRβ
Perlecan PDGFRβ
B
Pericyte coverage (%)
0.4
0.3
0.2
0.1
0
ns
+/+
+/G498V

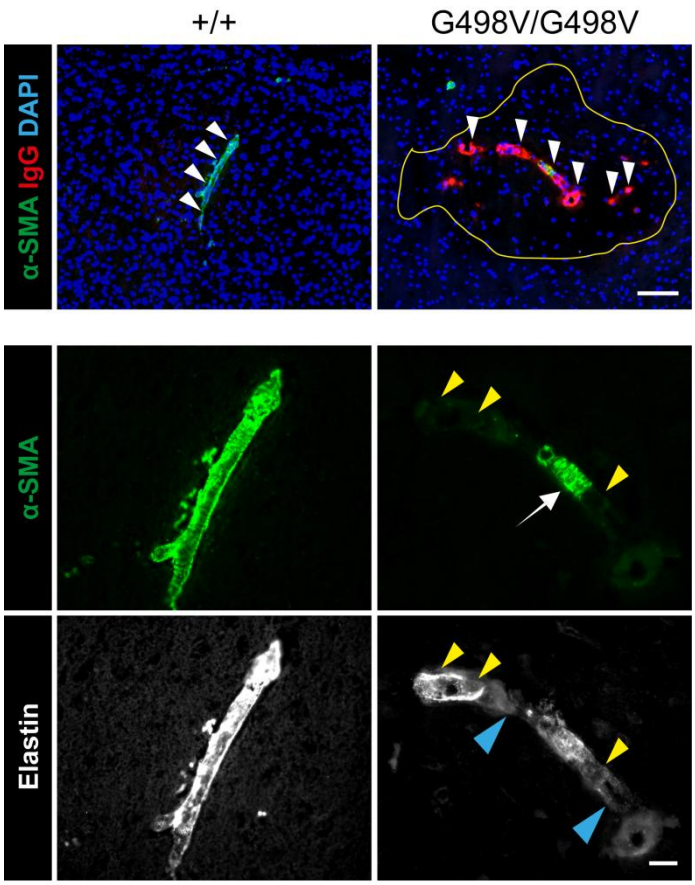
+/+
G498V/G498V
α-SMA IgG DAPI
α-SMA
Elastin

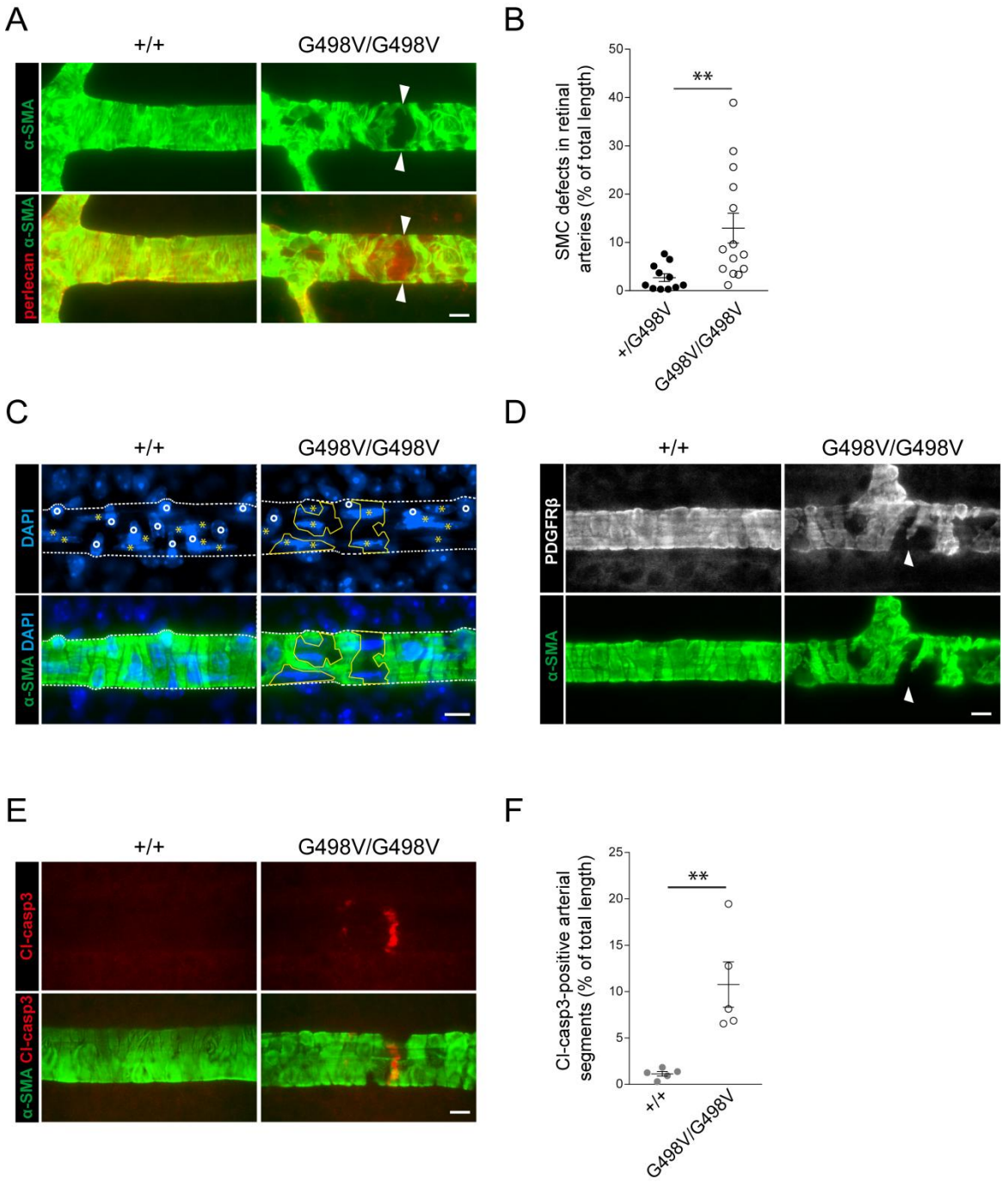
A
+/+
G498V/G498V
α-SMA
perlecan α-SMA
B
SMC defects in retinal arteries (% of total length)
**
+/G498V
G498V/G498V
C
+/+
G498V/G498V
DAPI
α-SMA DAPI
D
+/+
G498V/G498V
PDGFRβ
α-SMA
E
+/+
G498V/G498V
Cl-casp3
α-SMA Cl-casp3
F
Cl-casp3-positive arterial segments (% of total length)
**
+/+
G498V/G498V